AGU PUBLICATIONS

JGR

Journal of Geophysical Research: Solid Earth

RESEARCH ARTICLE
10.1002/2016JB013689

Key Points:
- Remotely generated seismic waves may destabilize accretionary margin sediment slopes
- Seafloor temperature and pressure measurements record sediment-laden gravity flows
- Small slope failures leading to gravity flows likely occur frequently along the Cascadia margin

Supporting Information:
- Supporting Information S1

Correspondence to:
H. P. Johnson,
paulj@uw.edu

Citation:
Johnson, H. P., J. S. Gomberg, S. L. Hautala, and M. S. Salmi (2017), Sediment gravity flows triggered by remotely generated earthquake waves, *J. Geophys. Res. Solid Earth*, *122*, doi:10.1002/2016JB013689.

Received 27 OCT 2016
Accepted 18 MAY 2017
Accepted article online 22 MAY 2017

©2017. American Geophysical Union. All Rights Reserved.

Sediment gravity flows triggered by remotely generated earthquake waves

H. Paul Johnson[1], Joan S. Gomberg[2,3], Susan L. Hautala[1], and Marie S. Salmi[1]

[1]School of Oceanography, University of Washington, Seattle, Washington, USA, [2]U.S. Geological Survey, Seattle, Washington, USA, [3]Department of Earth and Space Sciences, University of Washington, Seattle, Washington, USA

Abstract Recent great earthquakes and tsunamis around the world have heightened awareness of the inevitability of similar events occurring within the Cascadia Subduction Zone of the Pacific Northwest. We analyzed seafloor temperature, pressure, and seismic signals, and video stills of sediment-enveloped instruments recorded during the 2011–2015 Cascadia Initiative experiment, and seafloor morphology. Our results led us to suggest that thick accretionary prism sediments amplified and extended seismic wave durations from the 11 April 2012 M_w8.6 Indian Ocean earthquake, located more than 13,500 km away. These waves triggered a sequence of small slope failures on the Cascadia margin that led to sediment gravity flows culminating in turbidity currents. Previous studies have related the triggering of sediment-laden gravity flows and turbidite deposition to local earthquakes, but this is the first study in which the originating seismic event is extremely distant ($>$ 10,000 km). The possibility of remotely triggered slope failures that generate sediment-laden gravity flows should be considered in inferences of recurrence intervals of past great Cascadia earthquakes from turbidite sequences. Future similar studies may provide new understanding of submarine slope failures and turbidity currents and the hazards they pose to seafloor infrastructure and tsunami generation in regions both with and without local earthquakes.

Plain Language Summary Turbidites are marine landslides on continental margins that are known to be triggered by local earthquakes. When triggered over a wide area by a nearby earthquake, these mud slides can in turn cause local tsunamis to inundate nearby coastal areas. Recent data from 3 years of ocean bottom seismometer deployments on the Cascadia margin in the Pacific Northwest have demonstrated that turbidites can also be triggered by remote earthquakes, including a distant large magnitude earthquake on the Sumatra margin, over 13,000 km distant from the eastern Pacific Ocean.

1. Introduction

1.1. Motivation

A wide range of possible types of sediment-laden gravity flows can occur on continental margins, ranging from dilute nepheloid layers that leave little signature in the geological record [*Goldfinger et al.*, 2013] to massive debris slope failures that involve displacements of sediment blocks many tens of meters in dimension and/or numerous sediment-laden flows through channels spread across hundreds or thousands of kilometers [*Scholz et al.*, 2016]. Both types of failures endanger submarine telecommunication cables and infrastructure and transport significant sediment volumes. The latter failure type may result from strong seismic shaking generated by large or nearby earthquakes, providing records of paleoearthquakes in "turbidites" left when flows culminate and sediments settle rapidly [*Goldfinger et al.*, 2012]. This study documents likely triggering of slope failures, sediment gravity flows, and turbidite deposition along the continental margin of the Cascadia Subduction Zone (CSZ), by seismic waves from a remote earthquake, albeit occurring only over length scales of tens of kilometers and producing deposits not always easily interpreted in the geologic record. The primary observations we employ are seafloor temperature measurements, mostly those from the base of the continental slope where the signal of warm sediment-laden flows clearly stands out from background variability, along with collocated measurements and analyses of pressures, seismic waves, bathymetry, and video images. Our study suggests a new approach to assessing susceptibility and triggering of submarine slope failure and new understanding the continuous resurfacing of continental margins generally [*Sawyer and DeVore*, 2015], not only in active regions like the CSZ [*Goldfinger et al.*, 2000] but also along tectonically stable margins like the US Atlantic seaboard [*Heezen and Ewing*, 1952; *ten Brink et al.*, 2014].

1.2. Previous Observations of Sediment Gravity Flows

Each of the key processes we invoke in this study has precedents in the literature, and some of the key examples are summarized in this section. Here we define turbidity flows as one subtype within the broader class of sediment gravity flows, in which turbulence sustains sediment particles while in suspension within a fluid, and a turbidite refers to the resulting sediment deposit. Sediment-laden gravity flows have been observed to continue for days to months after the triggering event due to subsequent processes within the water column that keep sediment in suspension. When triggered by earthquake-generated seismic shaking, a semi-continuous flow of sediments may be caused by successive slope failures due to weakening by cycling loading and increased fluid pressures within the sediments [*Itou et al*., 2000; *Tripsanas et al*., 2004; *Seeber et al*., 2007; *Vangriesheim et al*., 2009; *Thomson et al*., 2010; *McHugh et al*., 2011; *Carter et al*., 2012; *Oguri et al*., 2013; *Ashi et al*., 2014]. Long-lasting sediment gravity flows, with durations of weeks to months, have been linked directly to a specific triggering earthquake (see section 4.1).

A cascade of multiple progressive slope failures has also been reported for laboratory models, where frequent small sediment-driven currents precede much larger ones [*Yamada et al*., 2010]. While significant differences exist, inferences about these submarine processes have been based on studies of more accessible terrestrial landslides [*Meunier et al*., 2007; *ten Brink et al*., 2009] and liquefaction events [*Biscontin et al*., 2004] which show that slope failure may occur days or months after the shaking ceases, all of which cannot be attributed to triggering by aftershocks alone [*Jibson et al*., 1994; *Qiu*, 2016]. However, seismically generated turbidity currents also appeared early in the scientific literature and included initiations that were delayed by many days after an initial trigger by a seismic event [*Heezen and Ewing*, 1952; *Kastens*, 1984]. Although different in scale, slope failures may have continued for hours as they nourished the turbidity current from the 1929 Grand Banks earthquake [*Piper et al*., 1999]. Finally, while terrestrial landslides often have length-of-runout/height ratios from 1 to 5 and relatively short runout distances of only a few kilometers or less [*Jibson*, 1996, 2007; *Talling et al*., 2013], marine sediment-laden gravity flows may have larger length/height ratios with runout distances that approach 100 km for even relatively small flows [*Talling et al*., 2013; *Xu*, 2011]. These occur in a diversity of locations suggesting that highly specialized conditions are not required to produce long runouts, specific examples include Japan [*Arai et al*., 2013; *Ashi et al*., 2014], Norway [*Jansen et al*., 2002], the Mediterranean Sea [*Canals et al*., 2006], Taiwan [*Carter et al*., 2012], and over many thousands of kilometers on the Bengal Fan, see a comprehensive summary in *Puig et al*. [2014].

1.3. Cascadia and the Cascadia Initiative

The Cascadia margin extends 1100 km along the coastline from Vancouver Island, British Columbia to Cape Mendocino, California, and westward from the coast to the abyssal plane where the Juan de Fuca, Explorer, and Gorda plates subduct beneath the North American plate (Figure 1) [*Johnson et al*., 2012]. Along the continental margin, a thick accretionary sediment wedge overlies the downgoing plates. The slope of the Cascadia accretionary wedge seafloor can exceed 20° locally, and large sediment fans, deeply incised canyons, and morphology indicative of widespread slope instability and erosion by mass wasting, turbidity flows, and related gravity flows provide evidence of widespread instability and sediment-laden gravity flows [*Goldfinger et al*., 2012].

The data we employed were collected as part of the 2011–2015 Cascadia Initiative (CI) experiment (Figure 1). During the first 3 years of this experiment, Ocean Bottom Seismographs (OBSs) were deployed for roughly 9 to 12 month intervals along most of the Juan de Fuca and Gorda segments of the CSZ.

Complete discussions of the Cascadia Initiative experiment and its instrumentation are found in *Toomey et al*. [2014] and *Morton and Bilek* [2015] and summarized here. The CI array utilized 60 OBSs from the Amphibious Array Facility (AAF) of the OBS Instrument Pool (OBSIP). All OBS instrument packages contained three-component seismometers and pressure sensors, and 35 of these 60 OBSs were equipped with trawl-resistant shields, designed to be deployed in water depths shallower than 1000 m. During the first 3 years of the 4 year CI experiment, a total of 280 AAF and WHOI-Keck OBS deployments and recoveries occurred at 168 individual sites along the Cascadia margin. While most of the pressure sensors were differential gauges, which are prone to large baseline drifts, the 25 Lamont Doherty Earth Observatory (LDEO) OBS instruments were equipped with more stable Paroscientific absolute pressure gauges, which also included quartz temperature sensors (Figure 1) designed for internal calibration. The temperatures recorded by the LDEO OBSs served as the

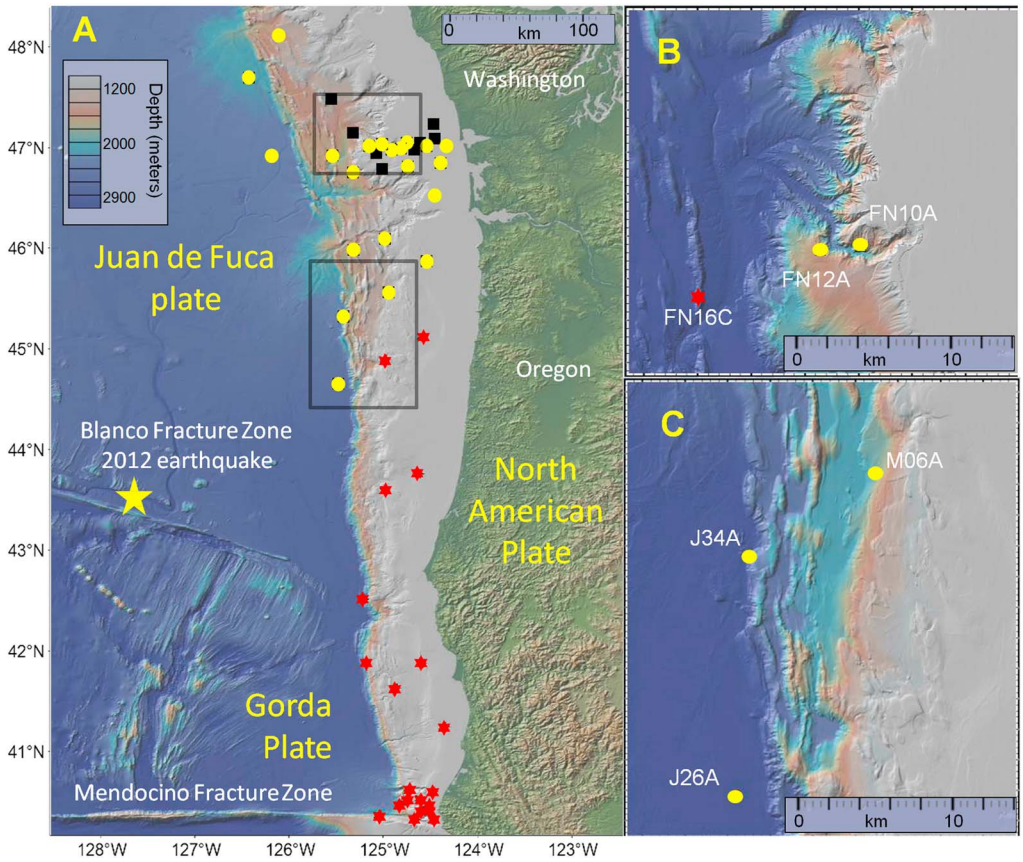

Figure 1. Seafloor and terrestrial topography of the U.S. portion of the Cascadia subduction zone: (a) LDEO OBS sites in deployments year 1 (23, yellow circles), year 2 (21, red 6-point stars), and year 3 (25, black squares). Yellow circles overlay black squares at sites occupied during both year 1 and year 3. The large five-point yellow star shows the epicenter of the 2012 M_w5.9 Blanco Fault Zone earthquake. The Gorda plate is bound by eastward extensions of the Blanco and Mendocino Fracture Zones. No well-defined trench exists at the western edge of the Cascadia Subduction Zone due to the thick infill of accretionary prism sediments; instead, the "deformation front" marks the boundary, where topography changes abruptly from the deformed prism toe (green-tinged shading) to the relatively featureless abyssal plain (darkest blues). Boxes show areas displayed in Figures 1b and 1c. (b) Bathymetry at OBS sites FN10A (instrument seafloor depth of 795 m), FN12A (650 m), and FN16C (1728 m) with temporally independent thermal anomalies. (c) Bathymetry at OBS sites J26A (2864 m), J34A (2574 m), and M06A (1439 m), where contemporaneous temperature anomalies were measured. Note that color scale change in Figures 1b and 1c from 1a.

basic data for this study. These data came from 23 LDEO OBS sites in year 1, 21 LDEO OBS sites in year 2, and 25 LDEO OBS sites in year 3, as shown in Figure 1a. The entire Cascadia Initiative OBS data set, including all sensor channels and site locations, is available on the Incorporated Research Institutions for Seismology (IRIS) website at http://ds.iris.edu/mda/7D?timewindow=2011-2017.

2. Observations

Here we present our identification of thermal anomalies at six of the total 69 deployed LDEO OBSs from CI years 1, 2, and 3 (Figure 2). We show swath bathymetry and backscatter images of these OBS sites, video images of the OBS recoveries at a small subset of sites where they are available, and examples of similar temperature signals observed on other continental margins are presented in section 3.1.2. We then describe our analyses of the pressure and seismic data recorded at these and other relevant OBS sites.

2.1. Temperatures

We identified thermal anomalies as signals where their amplitudes exceeded a three standard deviation (3σ) envelope of "background" water column temperature variability for each OBS, where σ was calculated from the start of the deployment period up to the onset of the larger-amplitude temperature variations that we

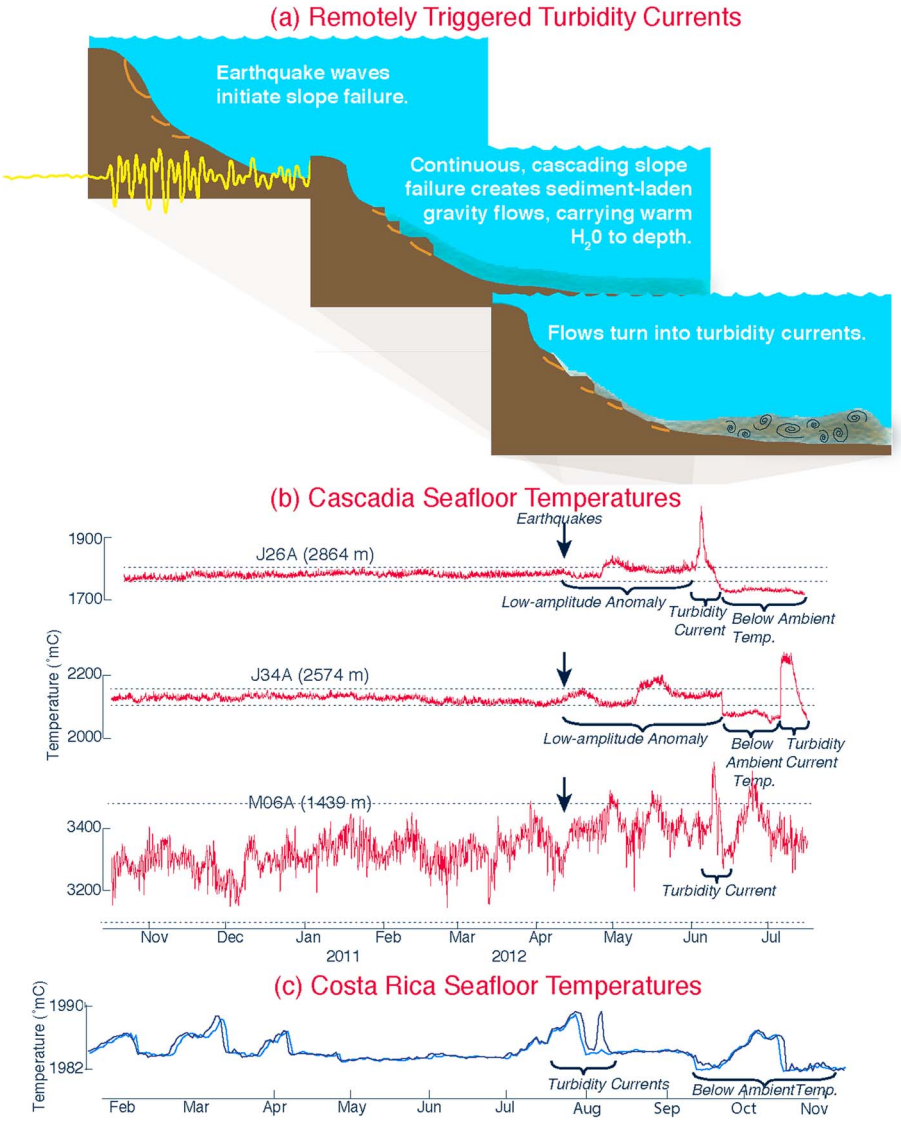

Figure 2. Temperature observations from Cascadia and Costa Rica and cartoon of explanatory model. (a) The hypothesized sequence of events that cause the temperature anomalies shown in Figure 2b; seismic waves destabilize slopes (upper left), failed slopes stir sediment into shallow warm waters causing them to flow downslope (middle), which gain density and speed and eventually turn into sediment-laden gravity flow (lower right). (b) Contemporaneous temperature signals recorded at adjacent LDEO OBS sites. Horizontal dotted lines show the temperature ranges that are three standard deviations from the mean. Ambient temperatures and noise levels increase as water depths shallow; locations of these sites, M06A, J34A, and J26A, are shown in Figure 1. Arrows denotes the ~14 h period on 11 April 2012 when the M_w8.6 and M_w8.2 Indian Ocean, and M_w5.9 Blanco Fracture Zone earthquakes occurred. (c) Temperature profiles recorded on the Costa Rico seafloor at two adjacent sites inferred to be manifestations of gravity currents, modified from Figure 4 of *Thomson et al*. [2010].

seek to understand. This noise envelope arises primarily from regular tidal variations, irregular variation in the 3–10 day frequency band related to atmospheric forcing, and additional lower frequency signals [*Hickey*, 1984; *McCabe et al*., 2015]. The amplitude of the background temperature variability decreases with increasing water depth, such that at sites on the abyssal plain, thermal excursions of +0.05°C stand out clearly above the 3σ background variability, indicated by dashed horizontal lines shown in Figure 2. Examination of temperature records from the 34 LDEO OBS sites deeper than 500 m water depth revealed a single period of time in which temperature anomalies at multiple sites appear at the adjacent OBS sites designated J26A, J34A, and M06A in the center of the Cascadia margin (Figures 1 and 2). We provide independent information confirming the reliability of the temperature measurements in the supporting information (Figure S1).

Records from J26A and J34A both show similar low-amplitude thermal anomalies lasting several months followed by large amplitude, warm pulses with durations of 2–10 days substantially exceeding 3σ in magnitude. These latter thermal "spikes" are followed by temperatures significantly lower than the preanomaly baseline. Because of its shallower depth (1430 m), M06A has higher background variability that could mask low-amplitude sediment gravity flow current signals, yet a temperature spike can arguably be detected in early June 2012. The nearly concurrent timing of abrupt temperature changes at J26A, J34A, and M06A and of low-amplitude anomalies at J34A and J26A (not resolvable at M06A) occurring for 1 to 2 months prior to these temperature spikes, adjacent spatial locations of all three sites, as well as other common features described below, may indicate a common causative mechanism. In contrast, subsequent deployment of instruments during year 3 at the same approximate locations as J26A and J34A shows no significant temperature anomalies (Figures S2 and S3).

In what follows, we focus on temperature signals at J26A and J34A due to a higher signal-to-noise ratio at these deeper stations and because the concurrence at two adjacent sites suggests a common source. However, we also identified three additional, but temporally and spatially isolated spikes on the northern portion of the CSZ, at sites FN10A, FN12A, and FN16C, which are similar to the anomaly observed at M06A (Figures 1 and S4).

2.2. Video Evidence of Sediment Deposition

Remotely Operated Vehicle (ROV) video images exist for sites shallower than 1000 m water depth, where OBS instruments were configured with Trawl-Resistant Mount (TRM) shields and required ROV submersible dives for recovery (A. Barclay, LDEO, personal communication, 2015). Thus, video images do not exist for the adjacent sites with thermal anomalies, J26A, J34A, and M06A, or for FN16C, the third isolated northern site with temperature anomaly. We visually examined all available ROV video still images, from sites with and without temperature anomalies, and found that only sites FN10A and FN12A showed clear evidence of postdeployment envelopment of mud that was several tens of centimeters thick (Figures 1 and S5).

2.3. Swath Bathymetry

High-resolution swath bathymetry surrounding J26A, J34A, and M06A provides contextual support for a slope failure hypothesis. All three sites with thermal anomalies are located within existing turbidite channels or on the steep flanks of anticlinal ridges. The J34A site is located within a well-defined narrow channel that lies west of a gap in the first large anticlinal ridge of the accretionary wedge (Figure 3). The J26A site lies on the abyssal plain within a broad, shallow north-south trending topographic valley directly adjacent to the toe of the accretionary prism. There is no bathymetric evidence that M06A is located directly within a turbidity current pathway, but the ridge immediately above the site has a steep slope angle of $>20°$. The bathymetry at FN16C, FN10A, and FN12A suggests that all of the OBS instruments showing anomalous temperatures were deployed on or adjacent to plausibly unstable slopes (Figure S5).

2.4. Pressures

Pressure sensors record changes in the height or density of the overlying water column and most of the signal results from processes such as tidal and atmospheric variations which were not of interest to this study. Thus, we adopted the differential analysis approach described in *Wallace et al*. [2016], where larger-scale water column pressure variations common to two nearby sites is removed by differencing their pressure signals. Sites J34A and J26A are sufficiently near to one another (26 km) and deep enough ($>$2000 m) that much of the normal background bottom water pressure variability should be common to both sites and thus can be strongly reduced by differencing the time series [*Davis et al*., 2006] (Figure 4). Tidal signals are first removed from the detrended pressures time series using the Matlab package "t-tide" [*Pawlowicz et al*., 2002]. The detided data are zero-phase bandpassed between 1.5 and 160 days using a Butterworth filter to remove any remaining high-frequency signals as well as very long period variability, likely caused by sensor drift. The pressure difference between the two sites is then calculated and examined for consistency with differential changes in near-bottom water column density at the two instruments.

2.5. Seismic Data

We analyzed the LDEO OBS seismic data for a variety of purposes. First, we sought to identify signatures of the gravity flow's mechanical disturbance or deposition of sediments on the sensor housings. Only the vertical component seismometers functioned sufficiently continuously for the duration of the temperature

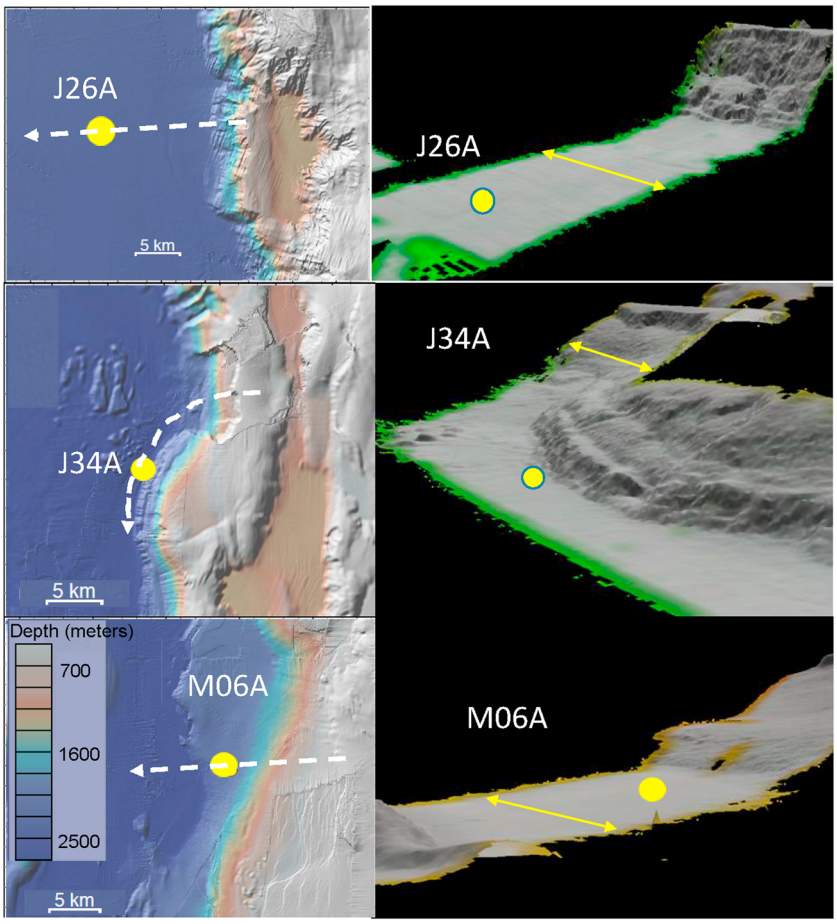

Figure 3. Bathymetric and acoustic backscatter images of sites M06A, J34A, and J26A. Site locations (yellow circles) (left column) atop bathymetry and (right column) 3-D rendering of the topography. White dashed lines indicate the center lines of the 3-D swath bathymetry. Yellow arrow scale bar is 3.5 km in horizontal dimension, and vertical exaggeration for draped images is 10:1. Suggested pathways shown are guided by slide scars and channels that predated any 2012 gravity flows but represent plausible flow paths located immediately upslope from the OBS deployment site.

anomalies at J26A, J34A, and M06A are useful, so we examined their outputs decimated to 1 min median values. We also examined these processed outputs from two of the other sites with temperature anomalies (FN12A and FN16A; no seismic data exist at FN10A) and from two sites with no temperature anomalies (Figure S6). We discuss the results and our interpretations in section 3.3.4.

We also visually examined spectrograms of seismic data recorded at J26A and J34A to look for evidence of tremor as an indication of slow slip or of any changes in spectral characteristics that might correlate with the onsets of the temperature anomalies (see section 3.4). No evidence of either process was observed, though the spectrograms are quite complex. Finally, we analyzed three-component seismograms of multiple distant and local earthquakes for the purpose of understanding the role of seismic waves on slope stability and discuss this in more detail in section 4.4.

3. Discussion

We conclude that the most plausible hypothesis explaining the temperature anomalies is that they are manifestations of sediment-laden gravity flows, initiated and fed by slope failures from the adjacent margin. In this section, we consider this and alternative hypotheses and describe the contextual and observational evidence used to evaluate the plausibility of each hypothesis. Relevant examples of studies of similar observations from the literature provide additional insights, and knowledge of ocean circulation offshore Cascadia provides further constraint on plausible hypotheses.

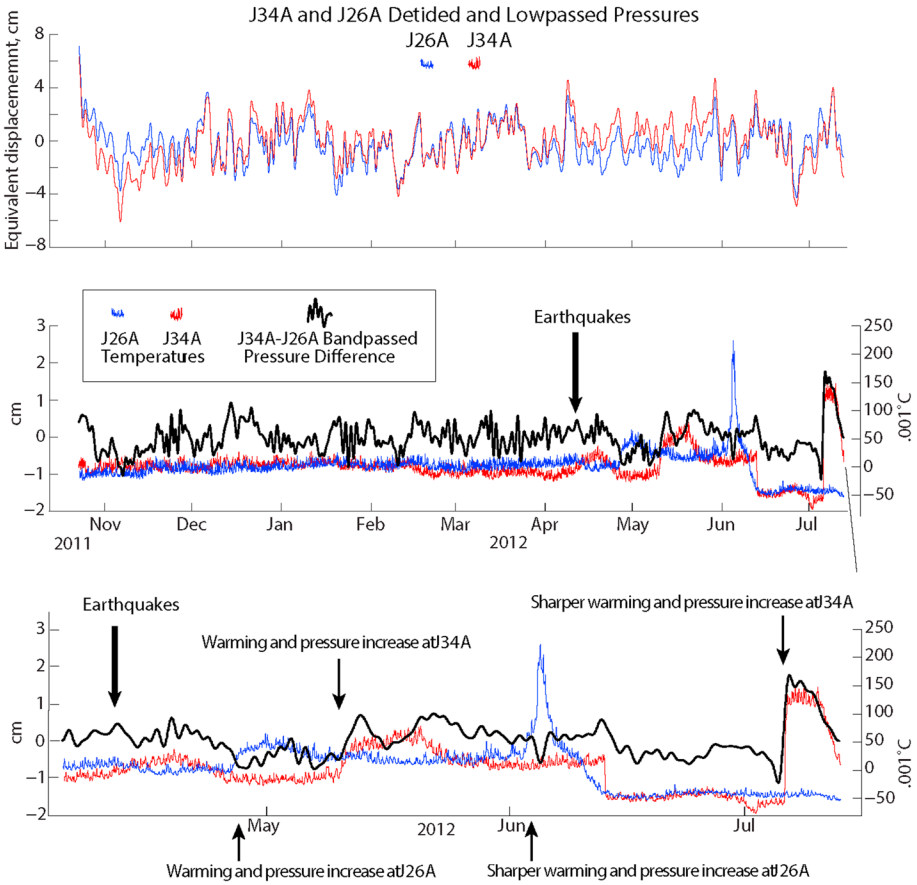

Figure 4. Temperatures and differenced pressures at J26A and J34A. Thicker arrow indicates time of the M_w8.6 and M_w8.2 Indian Ocean, and M_w5.9 Blanco Fracture Zone earthquakes. Pressure time series have been detided, (top) low passed, and (middle and bottom) band passed between 1.5 and 160 days prior to differencing. Pressures were converted to equivalent seawater depth changes or seafloor displacements. Signals for the entire deployment duration are shown in Figure 4 (top and middle), with an expanded and annotated window in Figure 4 (bottom). Episodes of warming and increased or reduced pressure difference are interpreted as the passage of dense sediment-laden flows at the corresponding sensor (see text).

3.1. An Example From the Literature

Data from the Middle America Trench of Costa Rica [*Thomson et al*., 2010] provide an example of how abyssal temperature records can be affected by sediment-laden gravity currents, showing rapid changes in temperature and pulse- or spike-like events (Figure 2). Despite their complex signatures, a striking similarity between the temperature anomalies at sites J26A and J34A to those off Costa Rica strongly suggests that the Cascadia instruments are also recording warm sediment-laden gravity flows. *Thomson et al*. [2010] interpret the temperature events in the Costa Rica data as manifestations of tidally generated gravity currents of denser water, sourced from an adjacent basin flowing over the southern sill of the trench, that increasingly entrained suspended sediments, scoured the seafloor, and ultimately produced erosive sediment-laden gravity currents (see Figure 2). The geographical setting of the Costa Rica instruments, located below sill depth in an ocean trench, differs considerably from the Cascadia setting located on the open abyssal plain, and we do not see evidence for regularly recurring tidally related water mass intrusions in our data. Still, the pulse-like nature of the temperature events at Costa Rica, a fingerprint of the passage of warm sediment-laden currents over the bottom sensors, is very similar to the events recorded at J26A and J34A.

3.2. Physical Constraints on the Process in the Cascadia Basin

Information from local conductivity, temperature, and depth (CTD) data, collected in 2006 [*Hautala et al*., 2009], allows us to estimate a conservative depth of origin for the turbidity currents associated with the

temperature spikes and to ascertain whether vertical displacement of the local temperature gradient at the seafloor by water column processes could plausibly explain the data. Depending on which CTD profile is used, reflecting the regional depth variation of temperature surfaces in the water column, we find maximum origin depths of 1890–1980 m for the J26A spike and 1665–1772 m for the J34A spike. These values imply a point of origin a minimum of 800 to 1000 m higher upslope from the sensors, with the real point of origin undoubtedly located considerably higher because of the strong mixing and entrainment associated with such flows. Vertical isotherm excursions of this magnitude are too large to result from regularly occurring water column processes, such as the passage of eddies, internal tides, or other baroclinic waves. Indeed, the background temperature variability in Figure 2 reflects such processes, with much smaller amplitude in the deep ocean where vertical temperature gradients are weak.

Also similar to the Costa Rica observations, temperatures at both the J26A and J34A sites following the temperature spike drop to values that are below preanomaly levels. *Thomson et al*. [2010] suggest that these temperature decreases are related to the reversal of pressure gradients along the seafloor that follow a buoyant "lift-off" of a hyperpycnal plume. The anomalous bottom currents associated with these pressure gradients replaced water in the warm bottom boundary layer with colder water located, in their case, to the northwest of their mooring. Again, although the geographical setting is different, a similar mechanism may also be responsible for the drop in temperatures that we observe following the observed thermal spikes. Along the Cascadia margin, a chronic geothermally heated bottom boundary layer is found east of Cascadia Sea Channel [*Hautala et al*., 2005, 2009]. Colder bottom water is located both to the south of this site in the Blanco Saddle and to the west in the Cascadia Sea Channel. Renewal of Cascadia Basin bottom water from these cold sources typically occurs over timescales of 2–3 years [*Hautala et al*., 2009]. Using the 2006 regional CTD data set, we estimate that advective renewal of the boundary layer during a convective flushing event that removes the heat associated with the chronic geothermal boundary and replaces it with colder water from either source region could plausibly account for the observed temperature drop given local currents of 5–10 cm/s. Although anomalous currents created by a very unusual upper ocean event, as discussed in more detail in section 3.4, or an independent abyssal water column renewal event are possible, such an occurrence would be singular within the 3 years of available OBS data, and the timing suggests an association with the events that precede it, rather than coincidence, as the most plausible explanation.

3.3. Evidence Supporting the Slope Failure-fed Gravity Flow Hypothesis

The information presented in sections 3.1 and 3.2 leads us to the hypothesis that the temperature anomalies observed result from warm seawater entrained from higher on the margin where slope failures occurred. In this section, we mention potential slope failure triggers (discussed at greater length in section 4) and summarize the contextual and observational evidence relevant to testing this hypothesis.

3.3.1. Contextual Evidence

The occurrence of slope failures shedding sediments into gravity-driven flows requires bathymetry with current pathways that connect plausibly steep, mechanically weak slopes to the OBS location. High-resolution swath bathymetry surrounding all sites with thermal anomalies provides contextual evidence for slope failures and sediment-laden currents (see section 2.3). All six sites with thermal anomalies are located within existing turbidity current pathways or downslope of credible zones of slope failures on the steep flanks of anticlinal ridges, where sediment mass transport from directly upslope is plausible.

As noted in section 2.2, the only sites with temperature anomalies (FN10A and FN12A) above 1000 m seafloor depth showed clear evidence of postdeployment envelopment by mud several tens of centimeters thick in ROV video images, provides further contextual evidence of the plausibility of slope failure leading to sediment-laden gravity flow hypothesis.

3.3.2. Temperature Signal Evidence

We propose the following chronology of sediment-laden gravity currents implied by the temperature signals at J34A, J26A, and M06A. At site J34A, the temperature spike that we attribute to the migration of a sediment-laden gravity flow arrives in early July 2012, approximately a month later than the large amplitude temperature anomaly that occurred at site J26A. We infer that the current that swept over J26A in June did not envelop J34A but disrupted the bottom water circulation pathways at both sites, resulting in postanomaly temperature decreases. Furthermore, the sediment-laden current arriving later at J34A also missed J26A, which implies the two OBS instruments are recording two distinct flows. Similar reasoning based on the

upper slope location of M06A suggests that at least three independent sediment-laden gravity flows in this region of the margin were captured by the array. It is also possible that the lower amplitude anomalies seen prior to the first spike in June in both OBS records represent anomalies from a later stage in the settling process of a separate event following a "leading edge" temperature spike that was not recorded in any of the instruments.

For an active gravity flow to produce the observed temperature anomalies requires that the sediment load must compensate buoyancy from warm water entrained at shallower depths and that the flow carries this less dense interstitial water down the slope, acting as a source of warm water to the bottom boundary layer at nearby sites on the abyssal plain. We estimate conservative lower bounds on the sediment volume fractions as those required to exactly compensate the warm water buoyancy when it arrives at the instruments on the abyssal plain, and note that the resulting fractions are plausible along the Cascadia margin. Following the method of *Thomson et al*. [2010], these minimum sediment volume fractions for the low-amplitude anomalies (~0.04°C) and spikes (~0.2°C) at J26A and J34A are 0.0004% and 0.002%, respectively, for a sediment density of clay of 2600 kg/m^3. Again, these sediment fractions should be viewed as very conservative lower bounds and correspond to no density or pressure anomaly at the seafloor associated with the turbidity current.

3.3.3. Pressure Signal Evidence

We examine the pressure data for further constraints on actual sediment concentrations, rather than just the aforementioned lower bounds. We also examine whether or not the observed pressure differences are consistent with a chronology of sediment gravity current arrival at the two sensors on the abyssal plain. At the time of the warm water spike at J26A in June, pressure at J34A is higher than at J26A (J34A $-$ J26A $>$ 0; Figure 4). A short-lived reduction in the pressure difference observed at these two locations has a timing consistent with the arrival of a sediment gravity current slightly denser than the ambient water at J26A. The pressure at J34A increases to a greater extent with the warm water spike in July, suggesting a denser sediment flow, consistent with its longer duration. For a 100 m thick layer, a plausible sediment concentration [*Meiburg and Kneller*, 2010] of 0.02% would be needed to produce the ~3 cm equivalent pressure change at this time. During the lower amplitude temperature events that precede these larger spikes, longer wavelength signals in the pressure difference are consistent with the arrival of warm sediment-laden plumes at different times at the two sites. Specifically, the pressure difference decreases when the temperature at J26A increases in late April and increases when a warm anomaly arrives at J34A in mid-May.

It is important to note that, unlike temperature, the amplitude of the pressure difference signal does not substantially exceed the background variability, and we cannot conclusively attribute its changes to dense currents arriving at the sensors; however, the sense of the variation is consistent with this mechanism. Following *Thomson et al*. [2010], for a turbid water column layer thickness of 100–200 m, the observed persistence of about 60 days for the earlier events is consistent with the settling velocity of particles with a 3 to 4.5 μm radius, suggesting that silt was the dominant constituent of the flows in late April and May. For the higher amplitude flows in June and July, a shorter decay timescale indicates somewhat larger grain sizes, but flow thickness and flow volumes are also important. We conclude that both the pressure and temperature data are consistent with plausible ranges of sediment concentration and grain sizes for sediment-laden gravity flows.

3.3.4. Seismic Signal Evidence

We searched for evidence of gravity flows jostling, or the deposition of sediments on the OBSs, in seismometer signals recorded at the five sites with both temperature anomalies and working seismographs (J26A, J34A, M06A, FN12A, and FN16C), as well as at two sites with no anomalies. The data processing is explained in section 2.5. Seismic signals show that the seismometers stopped recording ground motion several days prior to the abrupt changes in temperature at each site with temperature anomalies. However, this lag time of several days is perplexing, and explanation of it would be ad hoc at best. The seismic system at FN16C never recorded ground motion variations, but the DC level abruptly changed upon the arrival of the temperature anomaly. At FN12A, the seismic signal is extremely noisy throughout the deployment and does not correlate with the temperature signal. Finally, at the two sites with no temperature anomalies, the seismic systems recorded data throughout the entire deployment period. These observations strongly suggest to us a causative relation between the disruptions of the seismic systems and whatever lead to the abrupt temperature changes, which seems unlikely by chance, but the timing has sufficient uncertainties that we leave any judgment of significance to the reader.

3.4. Evaluation of an Upper Ocean Water Column/Storm Hypotheses

Upper ocean mesoscale processes may contribute to current variability on the seafloor [*Lavelle et al*., 2008; *Adams et al*., 2011], and the advection of background temperature gradients by such currents likely contributes to the observed envelope of background temperature variability in the OBS records. The fact that the thermal anomalies associated with the spikes greatly exceeds the amplitude of the background variability requires the presence of a water column event that is unusual in the record. We examined satellite data for evidence of such events. A distinct warming event in sea surface temperature does occur in mid-May 2012, at the same time as the second seafloor warming event at J34A (Figure S2). While it is tempting to attribute significance to this synchrony, National Data Buoy Center (NDBC) buoy data also show a warming event in the NE Pacific in late April, which appears even more prominently in the satellite sea surface temperature data (not shown) that correspond instead to seafloor cooling. Furthermore, a similar eddy warming event in late May 2014 is accompanied only by low level seafloor temperature changes (Figure S3).

We conclude that while it is possible that upper ocean mesoscale processes contribute to lateral migration of the warm bottom layer during late April to May of 2012, explaining its presence over the sensors at some times and colder background water at other times, the temperature increases and decreases associated with the larger temperature spikes in June and July are too rapid to be explained by these mechanisms. Given the 10 cm/s maximum current variation observed by *Adams et al*. [2011] associated with such events, a rise in temperature of 0.2°C over a few days would imply a comparable preexisting near-bottom temperature variation over lateral scales of a few tens of kilometers. However, temperature at the seafloor varies by only 0.1°C along the entire 433 km distance from 44.5 to 48.4°N in the chronic geothermally heated boundary layer east of Cascadia Sea Channel [*Hautala et al*., 2009]. A source of warm water to the seafloor near-bottom boundary layer is thus required to produce such rapid warming. Furthermore, since temperature anomalies were observed to occur at only 6 out of the 34 LDEO CI OBS sites below 600 m and episodes of such anomalies do not occur during the other two deployment years, it seems unlikely that these events can be explained by regularly occurring water column processes.

Hickey et al. [1986] conclude that on the Cascadia Margin storm-related resuspension events below 250 m depth occur very rarely, approximately once every 10 years. Similarly, *Snyder and Carson* [1986] show that any storm-related sediment transfer is limited to redistribution on the continental shelf with minor downslope transfer to the uppermost margin. We examined NDBC buoy data for evidence of unusual storm activity at the time of these anomalies. Wave height and atmospheric pressure time series do not show unusual storm events during this period, when compared to either earlier times in the same deployment or to 2013–2014 (Figures S2 and S3). Routine strength winter storm activity would have been expected to occur as frequently in years 2 and 3 (2012–2013 and 2013–2014) of the CI deployment as in year 1 (2011–2012), yet the anomalies exist only in year 1. Thus, we conclude that the likelihood that winter storms led to the sediment-laden gravity flows evident in the OBS data at J26A, J34A, and M06 is extremely low.

3.5. Evaluation of a Sediment Water-Expulsion Hypothesis

In this section, we consider a hypothesis in which some tectonic event caused contraction of prism sediments and consequent expulsion of the warm water recorded in the temperature data. There were no earthquakes large or near enough to the OBS instruments to deform the sediments, but sites J26A and J34A straddle the plate boundary where transient shallow slow slip may have occurred. For reasons noted in this section, this hypothesized mechanism may explain portions of the low-amplitude temperature and pressure signals, but it fails to explain the majority of the observations.

Slow slip on the shallow updip plate interface has previously been shown to produce clear temperature and pressure anomalies on the overriding plate in the Costa Rica [*Davis and Villinger*, 2006; *LaBonte et al*., 2009], Nankai, Japan [*Davis et al*., 2006], and Hikurangi, New Zealand [*Pouderoux et al*., 2012] subduction zones. These studies inferred that slow slip induced contraction and forced ejection of warm sediment pore water into the near seafloor water column from the accretionary prism sediments. If sufficiently large, geodetic evidence of transient shallow slip near the trench could be observed offshore and onshore. A recent shallow slow slip event in the Hikurangi subduction zone of New Zealand produced a reduction in offshore pressure equivalent to 1.5 to 5.4 cm of vertical seafloor uplift and onshore horizontal displacements of a few to ~15 mm [*Wallace et al*., 2016]. Similar studies of seafloor pressure and

onshore GPS measurements from Costa Rica infer slow slip transients propagated from beneath the locked zone to the toe of the accretionary prism.

No evidence of slow slip was reported in 2012 on Cascadia's onshore PANGA GPS network (http://www.geodesy.cwu.edu/realtime/). Slow slip of several centimeters on the plate interface should be resolvable if located beneath the CI OBS network, so this absence allows us to rule out slow slip along the Cascadia megathrust fault. However, shallow offshore slip of a centimeter or less would be difficult to resolve onshore, given Cascadia's greater separation between the prism toe and coast than in Costa Rica and Hikurangi.

We searched for seismic evidence of slow slip, manifesting as either tremor or increased earthquake rates, acknowledging that instrumental problems during the first year CI deployment may have elevated detection thresholds relative to other studies where such phenomena have been observed [*Morton and Bilek*, 2015]. We looked for tremor within the spectrograms of vertical component seismic signals (horizontal components recorded only for short intervals) at J34A, J26A, and M06A and found no clear signs of tremor. Increased seismicity rates sometimes accompany slow slip [*Davis et al*., 2006], but the only clear increase in activity within 100 km of J34A, J26A, and M06A was a cluster of a dozen $1.6 < M_w < 3.7$ earthquakes located in the middle of the margin that began in March 2012 [*Trehu et al*., 2015] long enough prior to the onset of the temperature anomalies and far enough from the prism deformation front to make suggestion of any correlation with slow slip highly speculative.

The observed differenced pressure signals from sites J26A and J34A could correspond to vertical seafloor motion of a few tens of millimeters up to a centimeter. Correlation between the differenced pressures (J34A-J26A) and temperature is greater at site J34A, as would be expected for slow slip compressing the sediments (Figures 1 and 4). The positive and negative excursions in the pressure differences imply a complex slip behavior, and the slip would need to continue for most of the several months duration of the anomalies in order to supply warm buoyant water throughout.

While slow slip-driven compression of prism sediments and expulsion of warm water may explain the gradual, low-amplitude temperatures, it cannot explain the large amplitudes and abruptness of the thermal spikes as the required warm water volumes are too large and expulsion rates too rapid. Fluid emissions from diffuse flow in nonfaulted sediment from subsurface overpressures, even with very thin sediment cover, have time constants for any change that are controlled by diffusion, with slow rise times and only localized emission sites [*Johnson et al*., 2000]. The near synchronicity of the abrupt changes in both the temperature at J34A and differenced pressures is also difficult to reconcile with qualitative estimates of slow diffusion of warm water from compacting sediments. Finally, a slow slip mechanism cannot explain the drops in ambient temperatures following the spike at J26A and sharp drop at J34A in early June.

3.6. Evaluation of a Trawling Hypothesis

Lastly, we can generally rule out nonseismic initiation of the sediment gravity currents by fishing trawls, as the topographically rough canyons located where the anomalous temperatures are observed are considered "hang spots" by the commercial fishing fleet and are not traditional areas for trawling. Trawling for bottom fish on the Cascadia margin is limited to water depths less than 1000 m, and all Oregon margin OBS instruments with identifiable thermal anomalies are at depths well below that limit.

4. Remotely Generated Seismic Wave-Triggered Slope Failure

Based on the hypotheses and evidence presented in section 3, the only hypothesis that explains all the observations is that a sequence of small, variably delayed slope failures culminates in sediment-laden gravity flows. In this section, we propose and demonstrate that cyclic loading and weakening of slope sediments by large-amplitude, long-duration seismic surface waves from the 2012 M_w8.6 earthquake in the Indian Ocean plausibly triggered the slope failures that led to the thermal anomalies at J26A, J34A, and M06A.

4.1. Evidence From the Literature

Examples of earthquakes with corresponding flow durations, which often represent minima determined by discrete sampling, include the M_w7.0 2010 Haiti (2 months [*McHugh et al*., 2011]) earthquake, the M_w7.4 1994 Sanriku-Oki (several months [*Itou et al*., 2000]), the M_w7.4 2004 off-Kii (2 weeks [*Ashi et al*., 2014]), and

the M_w9.0 2011 Tohoku-Oki (weeks [*McHugh et al*., 2016], 1 month [*Noguchi et al*., 2012], and 4 months [*Oguri et al*., 2013]) events near Japan. Gravity flows lasting 1–3 months in the Gulf of Mexico also have been attributed to an unknown seismic trigger [*Tripsanas et al*., 2004]. In a study of the M_w9.0 2011 Tohoku-Oki earthquake, turbidity currents generated by its tsunami and gravity flows resulted from shaking-induced slope weakening and failure that stirred sediment into the water column [*Arai et al*., 2013]. Data from sensors within a cabled observatory directly overlying the focal area of the 2003 Tokachi-Oki earthquake showed temperature anomaly amplitudes of approximately +0.5°C [*Mikada et al*., 2006], but these were attributed to turbidity flows that originated almost 4000 m higher in the water column than the sensors and would be expected to be of higher amplitude than our temperature anomalies with much shallower originating depths.

4.2. Seismic Wave Triggering of Other Failures

We suggest that if the seismic waves from the Indian Ocean earthquake were capable of triggering other types of natural failure processes, and with delays in some cases, so might they trigger slope failures along the Cascadia margin. In addition to the studies noted in section 1 that document delayed triggering by seismic waves in many environments, we add examples describing triggering by the Indian Ocean earthquake waves of $\geq M_w$5.5 earthquakes globally [*Pollitz et al*., 2012], of increased rates of tremor [*Chao and Obara*, 2016] and small earthquakes, strains, and seismic velocity changes in Japan [*Delorey et al*., 2015]. Almost all these triggered phenomena occurred with some delay, including a M_w5.9 earthquake on the Blanco Fracture Zone (BFZ) within the Cascadia Initiative footprint that occurred 14.1 h after the waves had passed [*Johnson and Bürgmann*, 2016].

4.3. Theoretical and Model Evidence

Models of submarine slope failures triggered by seismic waves invoke cyclic shearing that leads to accumulating plastic strain and shear-induced excess pore water pressure, decreasing the effective stress and leading to gravitational instability and failure [*Biscontin et al*., 2004]. Generally, slope failure initiation is more likely as the number of seismic cycles increases [*Biscontin et al*., 2004; *Talling et al*., 2014], and on continental margin slopes, failure results when sediment pore pressures elevate due to cyclic shearing until shear stress at failure drops below slope stress [*Meunier et al*., 2007; *Wang*, 2007; *Wang and Chia*, 2008]. Laboratory experiments show that seismic shaking also enhances sediment permeability, so that seismically induced excess pore pressures may migrate both vertically and horizontally and continue to increase long after the initial loading ceases. Depending on sediment type, the time to reach the excess peak pore pressures and then fully dissipate varies from minutes to decades [*Kokusho and Kojima*, 2002; *Biscontin et al*., 2004]. This may explain the observations of marine slope failures that initiate weeks to months after the initial triggering events [*Itou et al*., 2000; *McHugh et al*., 2011; *Noguchi et al*., 2012].

4.4. Cascadia Observations

4.4.1. Peak Strains and Energy Densities

To assess the plausibility of the hypothesis that seismic waves from the M_w8.6 Indian Ocean earthquake triggered Cascadia slope failures, we applied two metrics to the seismic waves recorded by CI OBS seismic sensors, to some of the largest and/or longest wave trains to affect the Cascadia margin (i.e., the distant M_w8.6 Indian Ocean, M_w8.2 Indian Ocean, M_w7.7 Haida Gwaii, British Columbia, 2014 M_w8.2 Iquique, Chile earthquake, and a local M_w5.9 event on the BFZ in 2012; Figures 5 and S7). In the absence of an established metric for quantifying likelihood of sediment slope failure due to cyclic loading, we adopt metrics applied to failures with similar causative mechanisms—liquefaction, deep-seated landslides, and earthquakes—and do not invoke strict thresholds or make detailed inferences. We suggest that if seismic wave shear energy can cause liquefaction, it also may be sufficient to trigger slope failure; e.g., seismic pumping and fluid pressure effects enhance the likelihood of marine slope failure and liquefaction, both of which have been implicated in turbidity current generation [*Goldfinger et al*., 2012]. We employ a total dissipated energy metric taken from liquefaction studies, which accounts for the duration of the waves and calculated as half the product of the density times the sum of the squared ground velocities [*Wang*, 2007; *Wang and Chia*, 2008]. Observations for real earthquakes indicate energy densities as low as 0.1 to 1.0 Joules/m^3 caused liquefaction, in some cases with significant delays. Experimentally derived failure threshold estimates range from ~0.1 to 10 J/m^3 with 30 J/m^3 appearing necessary for immediate liquefaction [*Wang*, 2007]. We also used peak strains

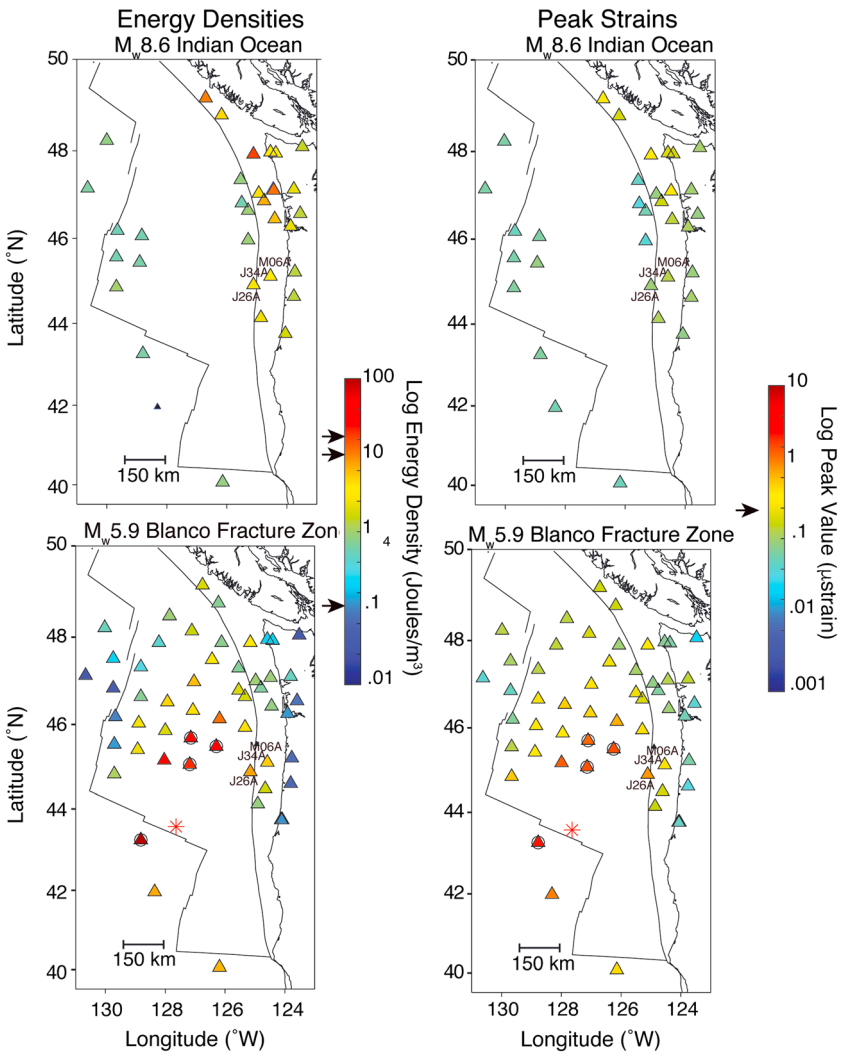

Figure 5. Seismic energy densities and peak strains for horizontal component waves from the M_w8.6 Indian Ocean and M_w5.9 Blanco Fracture Zone earthquakes. The asterisk in the lower maps indicates the epicenter of the latter. Triangles denote OBS locations, colored according to the measured energy density or peak strain (circled sites denote saturated signals). We show results for either the horizontal component oriented north-south or identified as component 1, noting that there is little overall difference if the other horizontal component is used, and vertical densities and peak strains are smaller and less affected by the prism sediments (Figure S7). Details of processing accompany Figure S6. (left column) Lower and central arrows at color bar indicate energy densities between 0.1 and 10 Joules/m^3 inferred sufficient to cause delayed liquefaction, and the top arrow indicates the threshold for immediate liquefaction. (right column) Peak strains equal peak velocities divided by an assumed shear wave velocity of 3 km/s [*Gomberg*, 2013].

as a metric, derived from measured peak seismic velocities, as this is often used to assess the potential for triggering liquefaction and landslides [*Wang*, 2007; *Wang and Chia*, 2008; *ten Brink et al*., 2014; *Jibson and Harp*, 2016], or earthquakes [*Pollitz et al*., 2012; *Johnson and Bürgmann*, 2016]. Typical peak Coulomb stress thresholds associated with seismic wave triggering of earthquakes may be as small as 1 to 10 kPa, or equivalently 0.1 to 1.0 microstrain [*Johnson and Bürgmann*, 2016].

Although the energy densities calculated for the local M_w5.9 earthquake on the BFZ waves exceeded those from the M_w8.6 Indian Ocean earthquake at two sites near J26A, J34A, and M06A, we note that the slope failures responsible for the temperature anomalies likely occurred kilometers upslope and the Indian Ocean earthquake waves supplied more energy to a broader portion of the margin (Figure 5). Additionally, the energy densities calculated for the Indian Ocean waves are likely underestimates

because we measured their duration only until waves from the M_w8.2 Indian Ocean event arrived 124.5 min later, even though amplitudes were still significant thereafter. Note that Figure S8 shows energy densities for both Indian Ocean events. These features suggest that the waves originating in the Indian Ocean were as, or more, effective triggers for slope failures than those from the M_w5.9 BFZ earthquake. We also consider peak strains and find that the M_w5.9 BFZ event produced waves with larger peak strains along the margin than the M_w8.6 Indian Ocean event, but a nearly identical M_w6.0 BFZ earthquake occurred about 2 months earlier and no immediate changes were observed in either the temperature or pressure data. This implies that total energy density is a more diagnostic measure of slope failure triggering potential and further supports the inference that the M_w8.6 Indian Ocean earthquake waves were most important in triggering slope failures.

The M_w8.6 Indian Ocean wave energy densities were sufficient to trigger slope failures all along the Cascadia prism, assuming the failure criterion noted in the previous paragraph (see Figure 5). However, energy densities in excess of the failure threshold are a necessary but are not likely a sufficient, condition for triggering slope failures. This follows from the observation that among five earthquake wave fields examined, those radiated by the M_w7.7 Haida Gwaii earthquake imparted both the largest peak motions and energy densities along the Cascadia margin (Figure S7), but no temperature anomalies associated with that event were detected. Numerous studies of dynamic failures, including earthquakes and tremor, triggered by seismic wave loading demonstrate that the conditions that must be satisfied, or equivalently the thresholds crossed, for triggering events are likely both site- and time-dependent [*Hill and Prejean*, 2015]. The ranges of energy densities and peak ground velocities required to cause liquefaction or landsliding cited above imply the same is true for most natural failure processes. Additionally, we do not know if undetected slope failures were triggered near J26A, J34A, and M06 at the time of the Haida Gwaii earthquake, because the event occurred during the second CI deployment when almost all of the instruments were deployed at more southern site locations offshore of Southern Oregon and Northern California. These observations highlight the importance of additional exploration of the characteristics of seismic wave fields and site conditions necessary to initiate weakening and failure, now possible with in situ observations from experiments like the Cascadia Initiative.

4.4.2. Sediment-Enhanced Failure Probabilities

To explain the observed Indian Ocean energy density variations, we suggest that the substantial thickness of Cascadia's accretionary prism leads to a significant prolonging of the duration of surface waves, amplified by the trapping and resonance of long-period energy. For all the wave fields recorded by the OBS instruments that were examined, waves originating from outside the region change dramatically within the prism, with the sediments trapping the energy, amplifying and extending their durations. In addition to map views of the energy densities (Figure S7), the waveforms alone clearly demonstrate these effects (Figure S8). Sediment amplification and elongation of seismic waves are commonly observed on land, and in several cases offshore within subduction zone accretionary prisms [*Guo et al*., 2016] and sediment-filled axial transform fault valleys [see *Gomberg*, 2013, and references therein]. While somewhat variable, the average across-strike thickness of wedge sediments varies north-south along the CSZ but generally increases from ~5 km at the deformation front to ~25 km at the coastline [*McCrory et al*., 2012]. The sediments along the abyssal plain on the incoming oceanic plate are significantly thinner, a few kilometer thickness in the north to less than 1 km in the south [*Johnson et al*., 2012].

5. Implications

A wide range of possible types of sediment-laden gravity flows can occur on the Cascadia continental margin in the Holocene, ranging from dilute nepheloid layers that would leave little signature in the geological record [*Snyder and Carson*, 1986; *Goldfinger et al*., 2013] to massive debris slope failures containing blocks of consolidated sediment that approach many tens of meters in size and would have overturned, buried, or destroyed the OBS instruments [*Paull et al*., 2003]. Examples of the intermediate scale of gravity flows that we are calling upon would have sufficiently small sediment grain size to remain suspended in the water column for months [*McHugh et al*., 2011, 2016] but could still produce a localized centimeter-scale discontinuity in the sediment record [*Oguri et al*., 2013]. These intermediate scale gravity flows and associated sediment suspensions would be capable of producing the observed thermal anomalies and leaving deposits only a few centimeters in thickness, while not destroying or overturning the OBS instrument package.

If our interpretations drawn from the first 3 years of Cascadia Initiative data are correct, keeping in mind the sparse distribution of OBS instruments, we conclude that small gravity flows, turbidity currents, and slope failures are very likely to occur at least annually on all segments of the Cascadia margin. This interpretation is consistent with previous observations of two mud turbidites off the southern Oregon coast that were not produced by earthquakes on the subduction thrust fault [*Goldfinger et al*., 2013]. Other studies of the Cascadia Subduction Zone have also found similar areas of sediment gravity flows that were apparently triggered independently of large local megathrust earthquakes [*Peterson et al*., 2013; *Graehl et al*., 2014].

The remotely triggered sediment gravity flows producing our thermal and pressure anomalies are likely to be small, with only a few tens of kilometers of runout distance, and clearly do not represent margin-wide failures equivalent to those created by local megathrust earthquakes. However, the importance of assessing susceptibility and triggering of slope failure is evident in documented massive submarine landslides not only in active regions like the CSZ [*Goldfinger et al*., 2000] but also along tectonically stable margins like the U.S. Atlantic seaboard [*Heezen and Ewing*, 1952; *ten Brink et al*., 2014]. Seafloor observations of remotely generated seismic waves and their impacts provide new tools for such assessments and for understanding the continuous resurfacing of continental margins generally [*Sawyer and DeVore*, 2015].

6. Conclusions

We interpret observations of thermal anomalies lasting for approximately 4 months at two OBS locations straddling the deformation front as manifestations of sediment-laden gravity flows nourished by a cascade of multiple slope failure events triggered by seismic waves from the M_w8.6 Indian Ocean earthquake (Figure 2). Temperature anomalies are evident excursions outside the regularly occurring water column processes that contribute to low level long-period temperature fluctuations. Anomalous temperatures rise above the background variability eventually culminating in large-amplitude spikes and abrupt sustained drops in temperatures below background soon after the arrival of large-amplitude long-duration seismic waves. A third large amplitude, warm-temperature spike is also observed in the period between these two, at an adjacent site located at shallower water depths, where greater background variability would obscure any low level anomalies. We have considered the concurrence and uniqueness of these anomalies among all the CI temperature signals, and a comprehensive suite of complementary observations with the predictions of numerous alternative explanatory hypotheses and found that all others provide incomplete or inconsistent explanations.

Other observations examined in this study include seismic and absolute pressure data recorded on the Cascadia margin seafloor, high-resolution seafloor bathymetry, acoustic backscatter surrounding all anomalous sites, and ROV Jason II video stills. Published literature also shows several examples from other regions of seismic shaking triggering delayed ground failure and sediment-laden gravity flows lasting weeks to months and traveling several tens of kilometers [e.g., *McHugh et al*., 2011; *Oguri et al*., 2013; *McHugh et al*., 2016]. Finally, seismic recordings of the wavefields of multiple distant earthquakes show that accretionary prism sediments act as a waveguide, amplifying and prolonging seismic shaking and enhancing their potential to destabilize slope sediments. Such remote triggering of slope failure and gravity flows has not been considered previously for slope and seismic hazard analysis.

Acknowledgments
All the Cascadia Initiative data employed in this study may be obtained from the Incorporated Research Institutions for Seismology Data Management Center at http://ds.iris.edu/ds/nodes/dmc/. The authors thank Brian Atwater, Doug Toomey, Leonardo Seeber, Ester Sumner, Andrew Barclay, and an anonymous reviewer for their comments, help, and suggestions. Anne Trehu provided the Antares data for Figure S1. Support was provided by NSF/GeoPRISM award 1339635 to H.P.J. and Department of Energy award DE-FE0013998 to H.P.J. and Evan Solomon. The processed data sets used in this study will be contributed to the GeoPRISM and NGDC databases, as required by NSF.

References

Adams, D. K., D. J. McGillicuddy, L. Zamudio, A. M. Thurnherr, X. Liang, O. Rouxel, C. R. German, and L. S. Mullineaux (2011), Surface-generated mesoscale eddies transport Deep-sea products from hydrothermal vents, *Science*, *332*(6029), 580–583, doi:10.1126/science.1201629.

Arai, K., et al. (2013), Tsunami-generated turbidity current of the 2011 Tohoku-Oki earthquake, *Geology*, *41*(11), 1195–1198, doi:10.1130/G34777.1.

Ashi, J., R. Sawada, A. Omura, and K. Ikehara (2014), Accumulation of an earthquake-induced extremely turbid layer in a terminal basin of the Nankai accretionary prism, *Earth Planets Space*, *66*(1), 51–59, doi:10.1186/1880-5981-66-51.

Biscontin, G., J. M. Pestana, and F. Nadim (2004), Seismic triggering of submarine slides in soft cohesive soil deposits, *Mar. Geol.*, *203*(3–4), 341–354, doi:10.1016/S0025-3227(03)00314-1.

Canals, M., P. Puig, X. D. de Madron, S. Heussner, A. Palanques, and J. Fabres (2006), Flushing submarine canyons, *Nature*, *444*(7117), 354–357, doi:10.1038/nature05271.

Carter, L., J. D. Milliman, P. J. Talling, R. Gavey, and R. B. Wynn (2012), Near-synchronous and delayed initiation of long run-out submarine sediment flows from a record-breaking river flood, offshore Taiwan, *Geophys. Res. Lett.*, *39*, L12603, doi:10.1029/2012GL051172.

Chao, K., and K. Obara (2016), Triggered tectonic tremor in various types of fault systems of Japan following the 2012 M_w8.6 Sumatra earthquake, *J. Geophys. Res. Solid Earth*, *121*, 170–187, doi:10.1002/2015JB012566.

Davis, E., and H. Villinger (2006), Transient formation fluid pressures and temperatures in the Costa Rica forearc prism and subducting oceanic basement: CORK monitoring at ODP sites 1253 and 1255, *Earth Planet. Sci. Lett.*, *245*(1–2), 232–244, doi:10.1016/j.epsl.2006.02.042.

Davis, E., K. Becker, K. Wang, K. Obara, Y. Ito, and M. Kinoshita (2006), A discrete episode of seismic and aseismic deformation of the Nankai trough subduction zone accretionary prism and incoming Philippine Sea plate, *Earth Planet. Sci. Lett.*, *242*(1–2), 73–84, doi:10.1016/j.epsl.2005.11.054.

Delorey, A. A., K. Chao, K. Obara, and P. A. Johnson (2015), Cascading elastic perturbation in Japan due to the 2012 M_w 8.6 Indian Ocean earthquake, *Sci. Adv.*, *1*(9), e1500468–e1500468, doi:10.1126/sciadv.1500468.

Goldfinger, C., L. D. Kulm, L. McNeill, and P. Watts (2000), Super-scale failure of the southern Oregon Cascadia margin, *Pure Appl. Geophys.*, *157*, 1189–1226.

Goldfinger, C., et al. (2012), Turbidite event history—Methods and implications for Holocene paleoseismicity of the Cascadia subduction zone, *U.S. Geol. Surv. Prof. Pap., 1661-F*, 170 pp. [Available at https://pubs.usgs.gov/pp/pp1661f/.]

Goldfinger, C., A. E. Morey, B. Black, J. Beeson, C. H. Nelson, and J. Patton (2013), Spatially limited mud turbidites on the Cascadia margin: Segmented earthquake ruptures?, *Nat. Hazards Earth Syst. Sci.*, *13*(8), 2109–2146, doi:10.5194/nhess-13-2109-2013.

Gomberg, J. (2013), Permanently enhanced dynamic triggering probabilities as evidenced by two $M \geq 7.5$ earthquakes, *Geophys. Res. Lett.*, *40*, 4828–4833, doi:10.1002/grl.50933.

Graehl, N. A., H. M. Kelsey, R. C. Witter, E. Hemphill-Haley, and S. E. Engelhart (2014), Stratigraphic and microfossil evidence for a 4500-year history of Cascadia subduction zone earthquakes and tsunamis at Yaquina River estuary, Oregon, USA, *Geol. Soc. Am. Bull.*, *127*(1–2), 211–226, doi:10.1130/B31074.1.

Guo, Y., K. Koketsu, and H. Miyake (2016), Propagation mechanism of long-period ground motions for offshore earthquakes along the Nankai trough: Effects of the accretionary wedge, *Bull. Seismol. Soc. Am.*, *106*, 1176–1197, doi:10.1785/0120150315.

Hautala, S. L., H. P. Johnson, and T. Bjorklund (2005), Geothermal heating and the properties of bottom water in Cascadia Basin, *Geophys. Res. Lett.*, *32*(6), L06608, doi:10.1029/2004GL022342.

Hautala, S. L., H. P. Johnson, and D. E. Hammond (2009), Bottom water circulation in Cascadia Basin, *Deep Sea Res., Part I*, *56*(10), 1688–1707.

Heezen, B. C., and M. Ewing (1952), Turbidity currents and submarine slumps, and the 1929 Grand Banks earthquake, *Am. J. Sci.*, *250*, 849–873.

Hickey, B. M. (1984), The fluctuating longshore pressure gradient on the Pacific northwest shelf: A dynamic analysis, *J. Phys. Oceanogr.*, *14*, 276–293.

Hickey, B. M., E. T. Baker, and N. B. Kachel (1986), Suspended particle movement in and around Quinault submarine canyon, *Mar. Geol.*, *71*, 35–83.

Hill, D. P., and S. G. Prejean (2015), Dynamic triggering, in *Treatise on Geophysics*, 2nd ed, vol. 4, edited by H. Kanamori, Elsevier, Oxford, U. K.

Itou, M., I. Matsumura, and S. Noriki (2000), A large flux of particulate matter in the deep Japan trench observed just after the 1994 Sanriku-Oki earthquake, *Deep Sea Res., Part I*, *47*, 1987–1998.

Jansen, E., S. Befring, T. Bugge, T. Eidvin, H. Holtedahl, and H. P. Sejrup (2002), Large submarine slides on the Norwegian continental margin: Sediments, transport and timing, *Mar. Geol.*, *78*, 77–107.

Jibson, R. W. (1996), Use of landslides for paleoseismic analysis, *Eng. Geol.*, *43*, 291–323.

Jibson, R. W. (2007), Regression models for estimating coseismic landslide displacement, *Eng. Geol.*, *91*(2–4), 209–218, doi:10.1016/j.enggeo.2007.01.013.

Jibson, R. W., and E. L. Harp (2016), Ground motions at the outermost limits of seismically triggered landslides, *Bull. Seismol. Soc. Am.*, *106*, 708–719, doi:10.1785/0120150141.

Jibson, R. W., C. S. Prentice, B. A. Borissof, E. A. Rogoshin, and C. J. Langer (1994), Some observations of landslides triggered by the 29 April 1991 Racha earthquake, Republic of Georgia, *Bull. Seismol. Soc. Am.*, *84*, 963–973.

Johnson, C., and R. Bürgmann (2016), Delayed dynamic triggering: Local seismicity leading up to three remote *M*6 aftershocks of the 11 April 2012 *M*8.6 Indian Ocean earthquake, *J. Geophys. Res. Solid Earth*, *121*, 134–151, doi:10.1002/(ISSN)2169-9356.

Johnson, H. P., M. Hutnak, R. P. Oziak, C. G. Fox, I. Urcuyo, J. P. Cowan, J. Nabelek, and C. Fisher (2000), Earthquake-induced changes in a hydrothermal system on the Juan de Fuca mid-ocean ridge, *Nature*, *407*, 174–177.

Johnson, H. P., S. L. Hautala, and T. A. Bjorklund (2012), The thermal environment of Cascadia Basin, *Geochem. Geophys. Geosyst.*, *13*, Q07003, doi:10.1029/2011GC003922.

Kastens, K. A. (1984), Earthquakes as a triggering mechanism for debris flows and turbidites on the Calabrian ridge, *Mar. Geol.*, *55*, 13–33.

Kokusho, T., and T. Kojima (2002), Mechanism for post-liquefaction water film generation in layered sand, *J. Geotech. Geoenviron. Eng.*, *128*, 129–137.

LaBonte, A. L., K. M. Brown, and Y. Fialko (2009), Hydrologic detection and finite element modeling of a slow slip event in the Costa Rica prism toe, *J. Geophys. Res.*, *114*, B00A02, doi:10.1029/2008JB005806.

Lavelle, J. W., G. J. Massoth, E. T. Baker, and C. E. J. de Ronde (2008), Ocean current and temperature time series at Brothers volcano, *J. Geophys. Res.*, *113*, C09018, doi:10.1029/2007JC004713.

McCabe, R. M., B. M. Hickey, E. P. Dever, and P. MacCready (2015), Seasonal cross-shelf flow structure, upwelling relaxation, and the along shelf pressure gradient in the northern California current system, *J. Phys. Oceanogr.*, *45*(1), 209–227, doi:10.1175/JPO-D-14-0025.1.

McCrory, P. A., J. L. Blair, F. Waldhauser, and D. H. Oppenheimer (2012), Juan de Fuca slab geometry and its relation to Wadati-Benioff zone seismicity, *J. Geophys. Res.*, *117*, B09306, doi:10.1029/2012JB009407.

McHugh, C. M., et al. (2011), Offshore sedimentary effects of the 12 January 2010 Haiti earthquake, *Geology*, *39*(8), 723–726, doi:10.1130/G31815.1.

McHugh, C. M., T. Kanamatsu, L. Seeber, R. Bopp, M.-H. Cormier, and K. Usami (2016), Remobilization of surficial slope sediment triggered by the A.D. 2011 M_w9 Tohoku-Oki earthquake and tsunami along the Japan trench, *Geology*, *44*(5), 391–394, doi:10.1130/G37650.1.

Meiburg, E., and B. Kneller (2010), Turbidity currents and their deposits, *Annu. Rev. Fluid Mech.*, *42*(1), 135–156, doi:10.1146/annurev-fluid-121108-145618.

Meunier, P., N. Hovius, and A. J. Haines (2007), Regional patterns of earthquake-triggered landslides and their relation to ground motion, *Geophys. Res. Lett.*, *34*, L20408, doi:10.1029/2007GL031337.

Mikada, H., K. Mitsuzawa, H. Matsumoto, T. Watanabe, S. Morita, R. Otsuka, H. Sugioka, T. Baba, E. Araki, and K. Suyehiro (2006), New discoveries in dynamics of an *M*8 earthquake-phenomena and their implications from the 2003 Tokachi-oki earthquake using a long term monitoring cabled observatory, *Tectonophysics*, *426*(1–2), 95–105, doi:10.1016/j.tecto.2006.02.021.

Morton, E. A., and S. L. Bilek (2015), Preliminary event detection of earthquakes using the Cascadia Initiative data, *Seismol. Res. Lett.*, *86*(5), 1270–1277, doi:10.1785/0220150098.

Noguchi, T., W. Tanikawa, T. Hirose, W. Lin, S. Kawagucci, Y. Yoshida-Takashima, M. C. Honda, K. Takai, H. Kitazato, and K. Okamura (2012), Dynamic process of turbidity generation triggered by the 2011 Tohoku-Oki earthquake, *Geochem. Geophys. Geosyst.*, *13*, Q11003, doi:10.1029/2012GC004360.

Oguri, K., K. Kawamura, A. Sakaguchi, T. Toyofuku, T. Kasaya, M. Murayama, K. Fujikura, R. N. Glud, and H. Kitazato (2013), Hadal disturbance in the Japan trench induced by the 2011 Tohoku–Oki earthquake, *Sci. Rep.*, *3*, 1–6, doi:10.1038/srep01915.

Paull, C. K., W. Ussler, H. G. Greene, R. Keaten, P. Mitts, and J. Barry (2003), Caught in the act: The 20 December 2001 gravity flow event in Monterey Canyon, *Geo-Mar. Lett.*, *22*(4), 227–232, doi:10.1007/s00367-003-0117-2.

Pawlowicz, R., B. Beardsley, and S. Lentz (2002), Classical tidal harmonic analysis including error estimates in MATLAB using T TIDE, *Comput. Geosci.*, *28*, 929–937.

Peterson, C. D., J. J. Clague, G. A. Carver, and K. M. Cruikshank (2013), Recurrence intervals of major paleotsunamis as calibrated by historic tsunami deposits in three localities: Port Alberni, Cannon Beach, and Crescent City, along the Cascadia margin, Canada and USA, *Nat. Hazards*, *68*(2), 321–336, doi:10.1007/s11069-013-0622-1.

Piper, D. J. W., P. Cochonat, and M. L. Morrison (1999), The sequence of events around the epicentre of the 1929 Grand Banks earthquake: Initiation of debris flows and turbidity current inferred from sidescan sonar, *Sedimentology*, *46*, 79–97.

Pollitz, F. F., R. S. Stein, V. Sevilgen, and R. Bürgmann (2012), The 11 April 2012 east Indian Ocean earthquake triggered large aftershocks worldwide, *Nature*, *490*, 250–253, doi:10.1038/nature11504.

Pouderoux, H., J.-N. Proust, G. Lamarche, A. Orpin, and H. Neil (2012), Postglacial (after 18 ka) deep-sea sedimentation along the Hikurangi subduction margin (New Zealand): Characterization, timing and origin of turbidites, *Mar. Geol.*, *295-298*(C), 51–76, doi:10.1016/j.margeo.2011.11.002.

Puig, P., A. Palanques, and J. Martín (2014), Contemporary sediment-transport processes in submarine canyons, *Annu. Rev. Mar. Sci.*, *6*(1), 53–77, doi:10.1146/annurev-marine-010213-135037.

Qiu, J. (2016), Listening for Landslides, *Nature*, *532*, 428–431.

Sawyer, D. E., and J. R. DeVore (2015), Elevated shear strength of sediments on active margins: Evidence for seismic strengthening, *Geophys. Res. Lett.*, *42*, 10,216–10,221, doi:10.1002/2015GL066603.

Scholz, N. A., M. Reidel, M. Urlaub, G. D. Spence, and R. D. Hyndman (2016), Submarine landslides offshore Vancouver Island along the northern Cascadia margin, British Columbia: Why preconditioning is like required to trigger slope failure, *Geo-Mar. Lett.*, *36*, 323–337.

Seeber, L., C. Mueller, T. Fujiwara, K. Arai, W. Soh, Y. S. Djajadihardja, and M.-H. Cormier (2007), Accretion, mass wasting, and partitioned strain over the 26 Dec 2004 Mw9. 2 rupture offshore Aceh, northern Sumatra, *Earth Planet. Sci. Lett.*, *263*(1), 16–31.

Snyder, G. W., and B. Carson (1986), Bottom and suspended particle sizes: Implications for modern sediment transport in Quinault submarine canyon, *Mar. Geol.*, *71*(1–2), 85–105.

Talling, P. J., C. K. Paull, and D. J. W. Piper (2013), How are subaqueous sediment density flows triggered, what is their internal structure and how does it evolve? Direct observations from monitoring of active flows, *Earth Sci. Rev.*, *125*(C), 244–287, doi:10.1016/j.earscirev.2013.07.005.

Talling, P., M. Clare, M. Urlaub, E. Pope, J. Hunt, and S. Watt (2014), Large submarine landslides on continental slopes: Geohazards, methane release, and climate change, *Oceanography*, *27*(2), 32–45, doi:10.5670/oceanog.2014.38.

ten Brink, U. S., H. J. Lee, E. L. Geist, and D. Twichell (2009), Assessment of tsunami hazard to the U.S. East Coast using relationships between submarine landslides and earthquakes, *Mar. Geol.*, *264*(1–2), 65–73, doi:10.1016/j.margeo.2008.05.011.

ten Brink, U. S., J. D. Chaytor, E. L. Geist, D. S. Brothers, and B. D. Andrews (2014), Assessment of tsunami hazard to the U.S. Atlantic margin, *Mar. Geol.*, *353*(C), 31–54, doi:10.1016/j.margeo.2014.02.011.

Thomson, R. E., E. E. Davis, M. Heesemann, and H. Villinger (2010), Observations of long-duration episodic bottom currents in the middle America trench: Evidence for tidally initiated turbidity flows, *J. Geophys. Res.*, *115*, C10020, doi:10.1029/2010JC006166.

Toomey, D., et al. (2014), The Cascadia Initiative: A sea change in seismological studies of subduction zones, *Oceanography*, *27*(2), 138–150, doi:10.5670/oceanog.2014.49.

Trehu, A. M., J. Braunmiller, and E. Davis (2015), Seismicity of the central Cascadia continental margin near 44.5 N: A decadal view, *Seismol. Res. Lett.*, *86*(3), 819–829, doi:10.1785/0220140207.

Tripsanas, E. K., W. R. Bryant, and B. A. Phaneuf (2004), Depositional processes of uniform mud deposits (unifites), Hedberg Basin, northwest Gulf of Mexico: New perspectives, *Am. Assoc. Pet. Geol. Bull.*, *88*, 825–840.

Vangriesheim, A., A. Khripounoff, and P. Crassous (2009), Turbidity events observed in situ along the Congo submarine channel, *Deep Sea Res., Part II*, *56*(23), 2208–2222, doi:10.1016/j.dsr2.2009.04.004.

Wallace, L. M., S. C. Webb, Y. Ito, K. Mochizuki, R. Hino, S. A. Henrys, S. Y. Schwartz, A. T. Sheehan, and A. F. Sheehan (2016), Slow slip near the trench at the Hikurangi subduction zone, New Zealand, *Science*, *352*(6286), 701–704, doi:10.1126/science.aad9521.

Wang, C.-Y. (2007), Liquefaction beyond the near field, *Seismol. Res. Lett.*, *78*, 512–517.

Wang, C.-Y., and Y. Chia (2008), Mechanism of water level changes during earthquakes: Near field versus intermediate field, *Geophys. Res. Lett.*, *35*, L12402, doi:10.1029/2008GL034227.

Xu, J. P. (2011), Measuring currents in submarine canyons: Technological and scientific progress in the past 30 years, *Geosphere*, *7*(4), 868–876, doi:10.1130/GES00640.1.

Yamada, Y., Y. Yamashita, and Y. Yamamoto (2010), Submarine landslides at subduction margins: Insights from physical models, *Tectonophysics*, *484*(1–4), 156–167, doi:10.1016/j.tecto.2009.09.007.

Journal of Geophysical Research – Solid Earth

Supporting Information for

Sediment Gravity Flows Triggered by Remotely-generated Earthquake Waves

H. Paul Johnson[1], Joan S. Gomberg[2, 3], Susan L. Hautala[1], Marie S. Salmi[1]

[1]School of Oceanography, University of Washington, Seattle WA 98195, [2]U.S. Geological Survey, [3]Department of Earth and Space Sciences, University of Washington Seattle, WA 98195

Contents of this file

Figures S1 to S9

Introduction

Figures in this Supplement include additional supporting analyses of the temperature, pressure and seismic data from the ocean bottom seismograph (OBS) systems, video frame grabs of the instrument deployment sites, and further analysis of the energy densities of the Indian Ocean and Blanco Fracture Zone earthquakes recorded by the Cascadia Initiative OBS instruments. Also included is a comparison between the Paroscientific temperature sensor with and external Antares temperature sensor during year 1 of the OBS deployment.

Figure S1

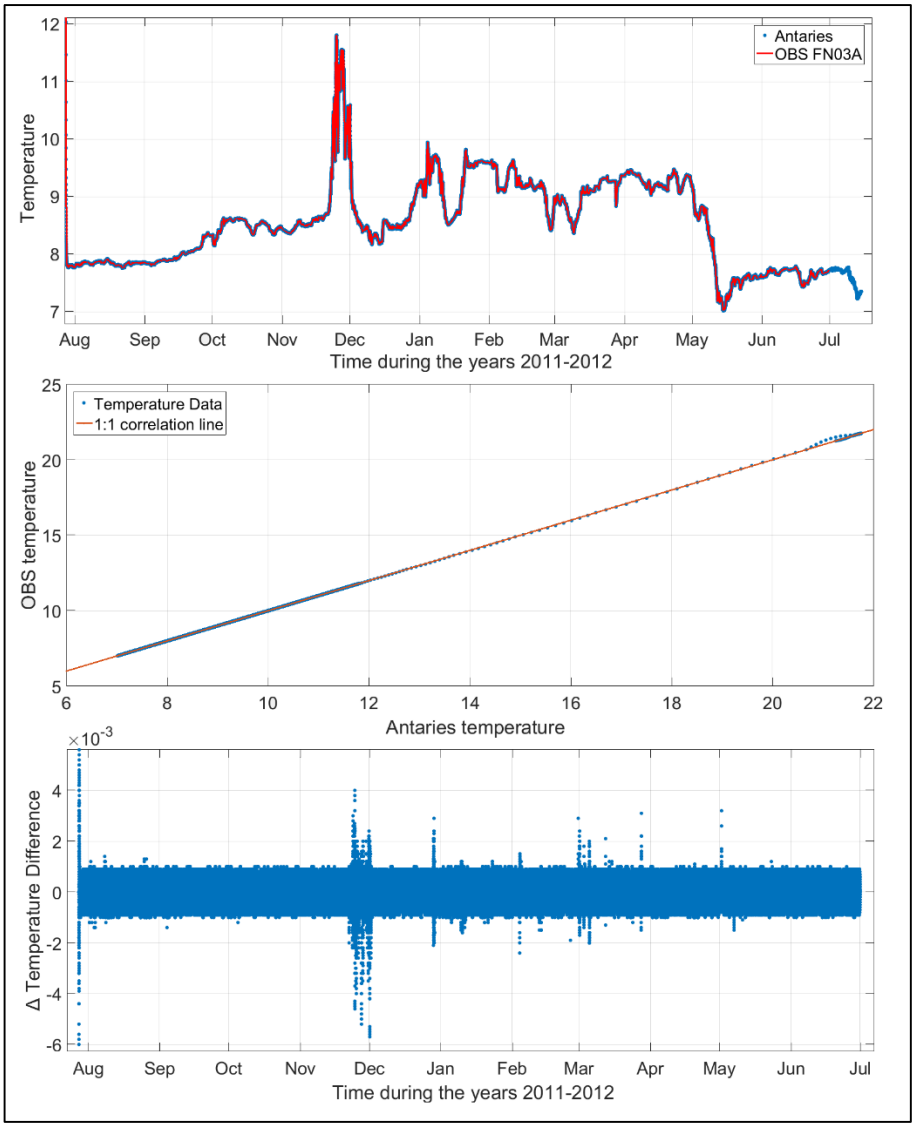

Figure S1. Independent validation of OBS temperatures. **(a)** Comparison of temperatures recorded at FN03A, at 90 m water depth on the Washington continental shelf, by the OBS sensors with those from an attached exposed Antares logger. Temperature sensors were calibrated separately. Temperature spike in late November recorded with both sensors is likely due an atmospheric event on the Washington coast. **(b)** Correlation between temperatures recorded by the Antares and OBS sensors at FN03A over a wide range of temperatures; the overlying orange line is the 1:1 relation. **(c)** Temperature difference between Antares and OBS temperature sensors as a function of time during the deployment of FN03A. Noise band shown is the ±1 millidegree C maximum resolution of the Antares A/D converter. Spikes in the difference during the November storm are likely due to the delay time between the exposed Antares sensor and the OBS sensor inside the APG pressure housing during rapidly varying temperatures.

Figure S2

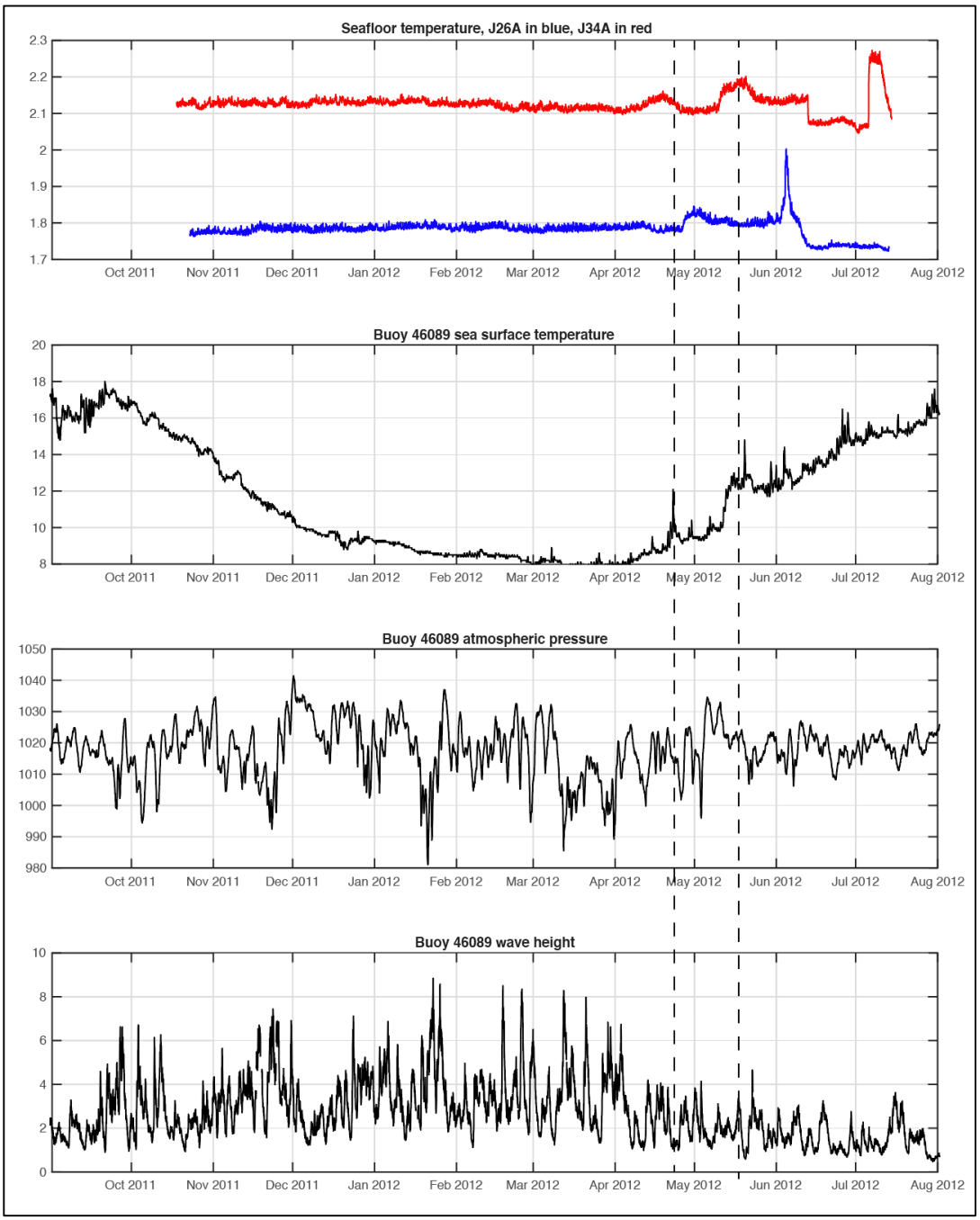

Figure S2. 2011/2012 deployment comparison between seafloor and upper ocean records. Top panel: temperature in °C recorded by J26A (blue) and J34A (red). Second panel: Hourly average sea surface temperature in °C recorded by NDBC buoy 46089, located at 45.893°N, 125.819°W in 2293 meter water depth. Third panel: Hourly average atmospheric pressure in hPa from the same buoy. Bottom panel: Hourly average wave heights from the same buoy. The two dashed lines mark two periods of anomalously warm sea surface temperature in spring 2012.

Figure S3

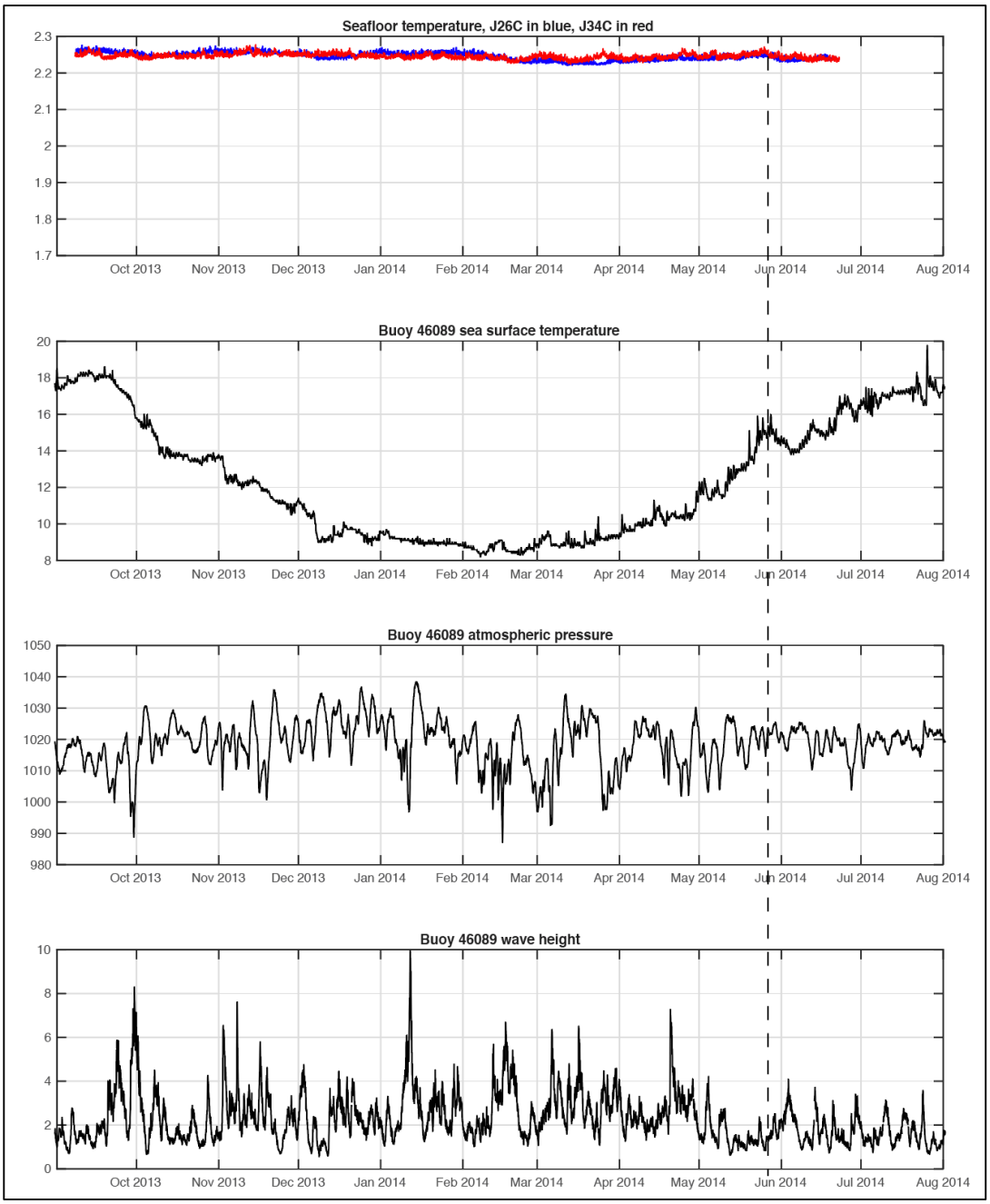

Figure S3. 2013/2014 deployment comparison between seafloor and upper ocean records. Top panel: temperature in °C recorded by J26C (blue) and J34C (red). Second panel: Hourly average sea surface temperature in °C recorded by the NDBC buoy 46089 located at 45.893°N, 125.819°W in 2293 m water depth. Third panel: Hourly average atmospheric pressure in hPa from the same buoy. Bottom panel: Hourly average wave height from the same buoy. The dashed line marks a period of anomalously warm sea surface temperature in Spring 2014.

Figure S4

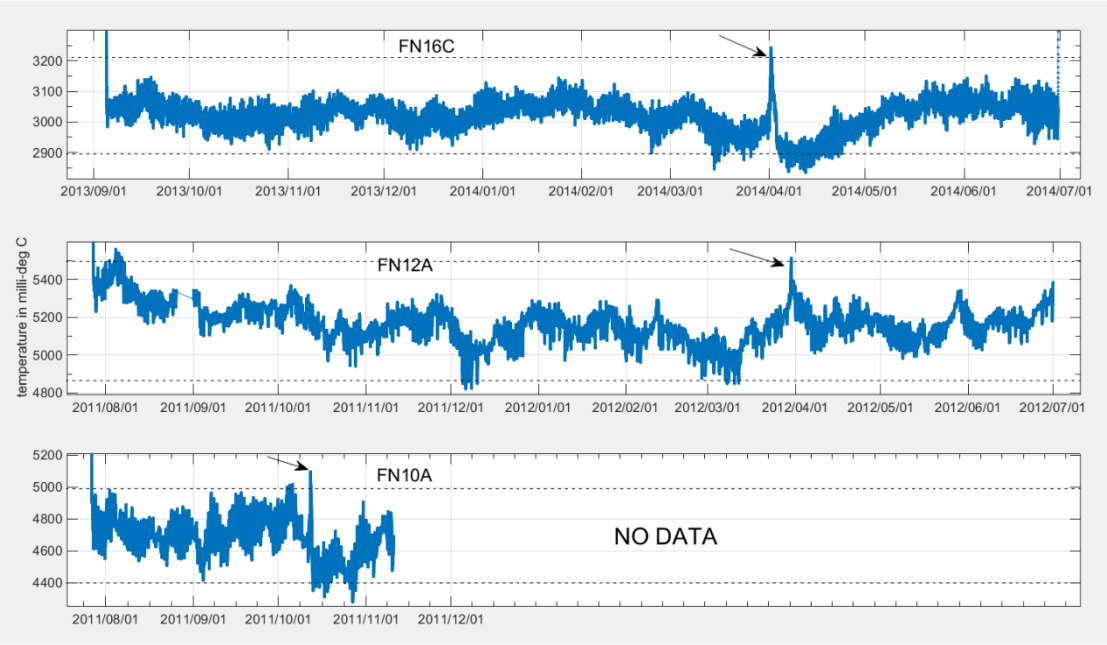

Figure S4. Temperature data from the 3 northern Cascadia LDEO OBS sites with isolated thermal anomalies. Temperature time-series for FN16C (top), FN12A (middle), and FN10A (bottom) with arrows indicating temperature anomalies. End of deployment ROV Jason II images (see Fig. S5) of OBS FN12A at the shallower depth of 650 meters shows mud enveloping the frame base. At FN10A, at 795 meters water depth, ROV Jason II video stills on recovery also showed envelopment of the OBS frame with mud and an abrupt end of data acquisition on 2011/11/9, long before OBS recovery. Horizontal dotted lines show the temperature ranges that are three standard deviations from the mean. The peak occurring during the initial deployment is residual heat entrained by the instrument during deployment through the water column.

Figure S5

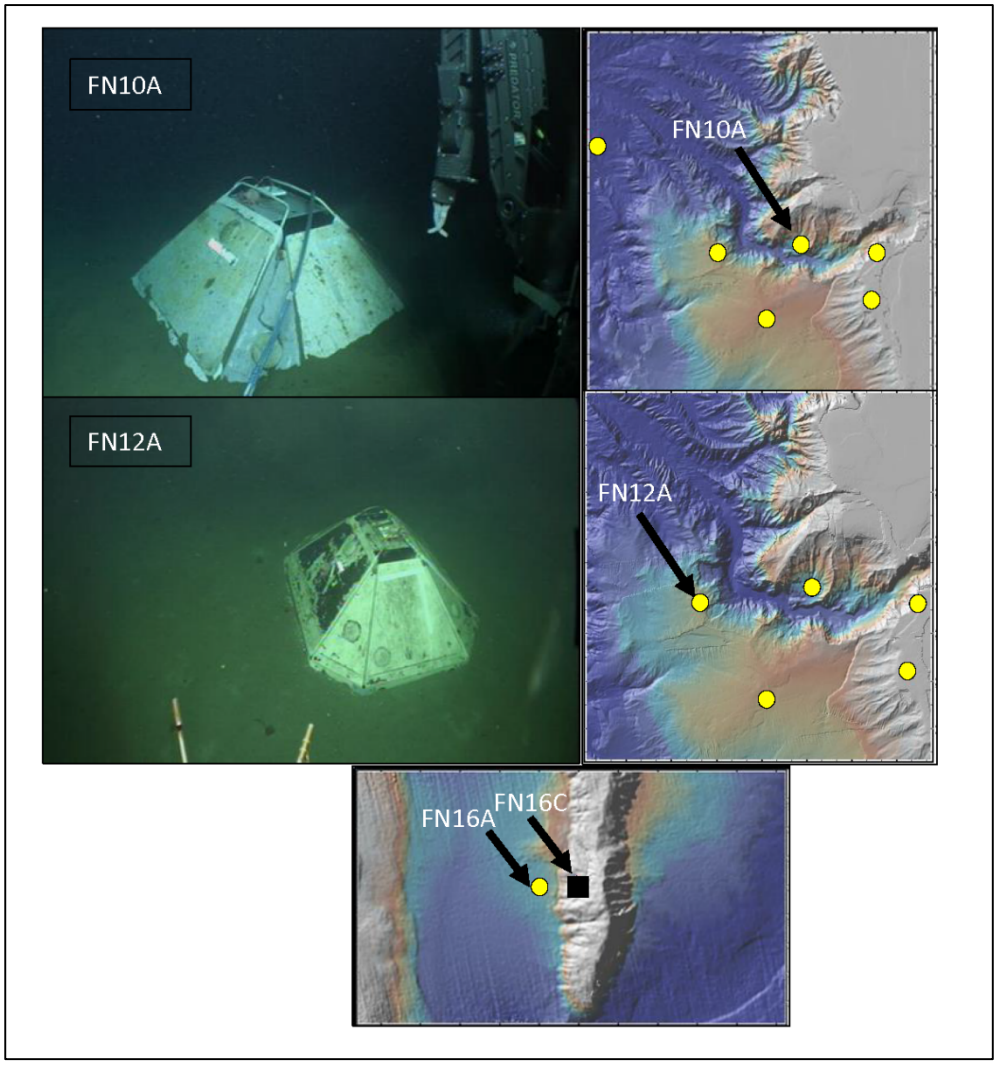

Figure S5. Jason II still images of OBS FN10A (top left) and FN12A (middle left) showing envelopment of the base by a turbidite. For scale, the dimension of the vertical base of the OBS is 47 cm, which is completely sediment covered in FN10A. It is possible that the sediment-covering of the base could have occurred during deployment onto a soft mud bottom instead of a post-deployment sediment gravity flow. Bathymetric images (Top/central right panels) show topography surrounding deployments (OBS sites shown by yellow circles and arrows). All sensors at FN10A (top right) failed 2011/11/9 (see Fig. S4), long before recovery and is at the base of a slump feeding Grays Canyon where rough topography would prevent disturbance by fishing trawls but not landslides, FN12A (middle right) is outside of a pre-existing turbidite channel, at a water depth 650 meters, with a temperature anomaly on 2012/3/30, prior to the Indian Ocean earthquake. FN16C (bottom panel) with thermal anomaly on 2014/ 4/1, was located on the western flank of an anticlinal ridge. The adjacent OBS site (yellow dot) is FN16A which had no thermal anomalies during the Year 1 deployment period. are shown in Figure S2.

Figure S6

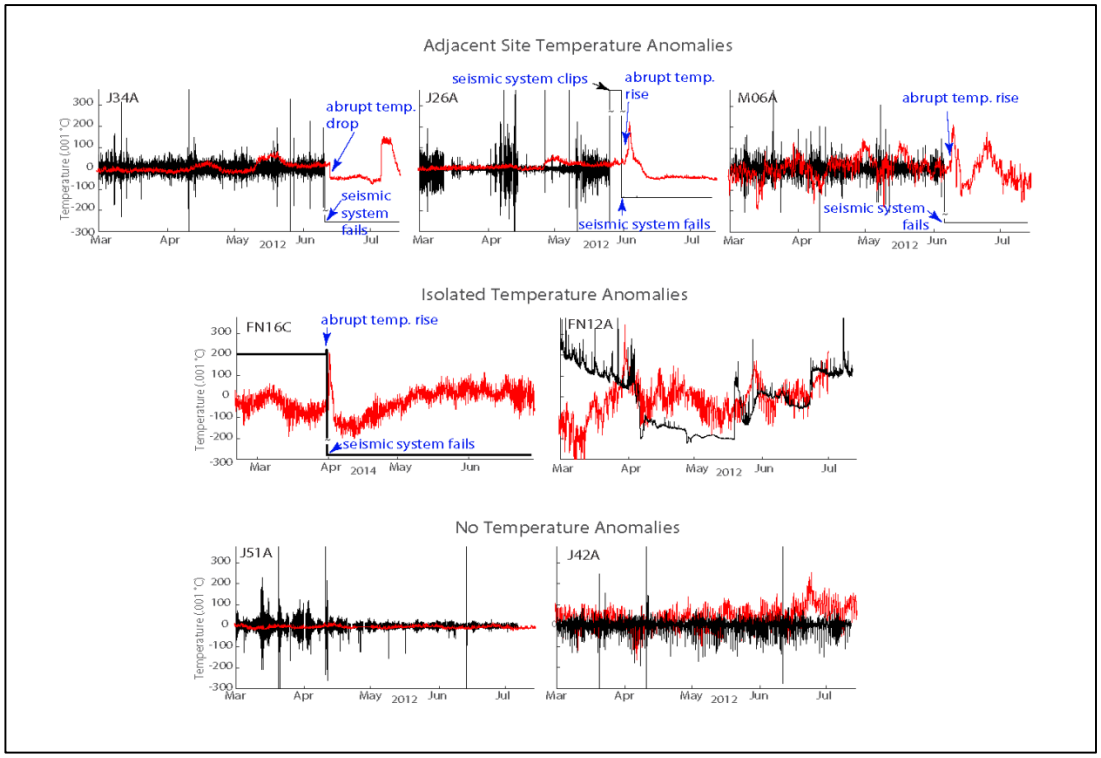

Figure S6. Seismic and temperature data from OBS instruments with (J34A, J26A, M06A, FN16C, and FN12A) and without (J51A and J42A) anomalies. Temperatures (red) and vertical component ground velocities decimated to 1-minute median values (black) at the three sites with contemporaneous temperature anomalies (top row, J34A, J26A, and M06A), at two of the three sites with isolated anomalies (middle row, FN16C and FN12A; no data exist for FN10A), and at sites with no temperature anomalies (bottom row). Tildes on seismic traces show where data saturated, and all seismic data are scaled differently, to highlight ground motions when recorded; y-axes show true demeaned temperatures. Annotations (blue) summarize the mode and chronology of seismic system malfunctions and significant temperature changes; no failures occurred at the two sites without temperature anomalies.

Figure S7

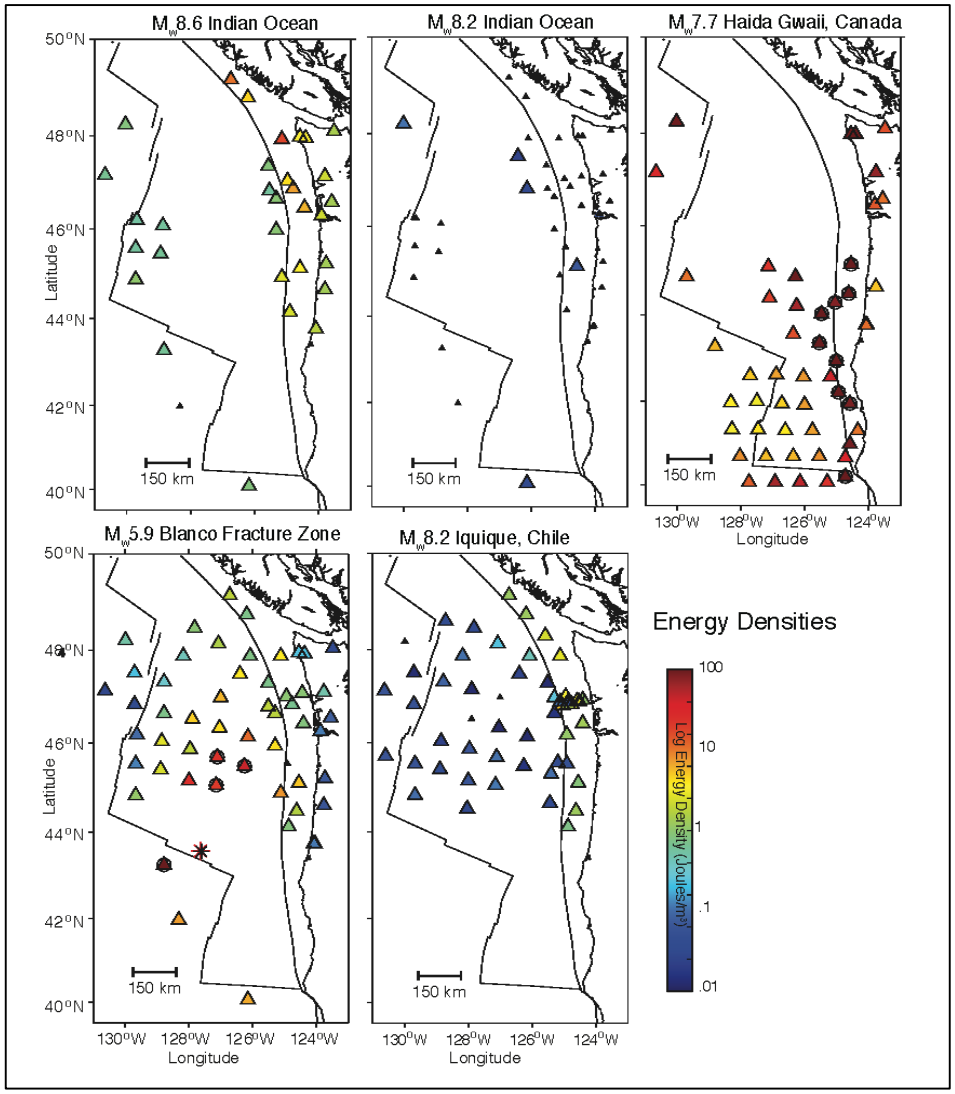

Figure S7. Energy densities for some of the largest and longest duration wave fields recorded during the CI experiment. Triangles denote OBS locations, colored according to the measured energy density or peak strain (circled sites denote saturated signals). Tiny triangles denote densities smaller than the color bar permits. Note that when the waves originate outside the region, the sites on the accretionary prism record the most energetic signals. The distribution of energy for the Blanco Fracture Zone earthquake (epicenter shown by the asterisk) is dominated by the rapid near-field decay rate, but sediment amplification and elongation at prism sites is still apparent (i.e. compare sites equidistant from the source on and off the prism). We show results for either the horizontal component oriented North-South or identified as component 1. All seismograms have had the instrument response deconvolved, were filtered in the frequency domain with a 4-corner cosine taper from .001 to .01 Hz and 1 to 5 Hz, and output as velocities. Durations were calculated as the interval between the P-wave arrival and when the rms signal level in a 10-minute interval equaled that of the pre-event background.

Figure S8

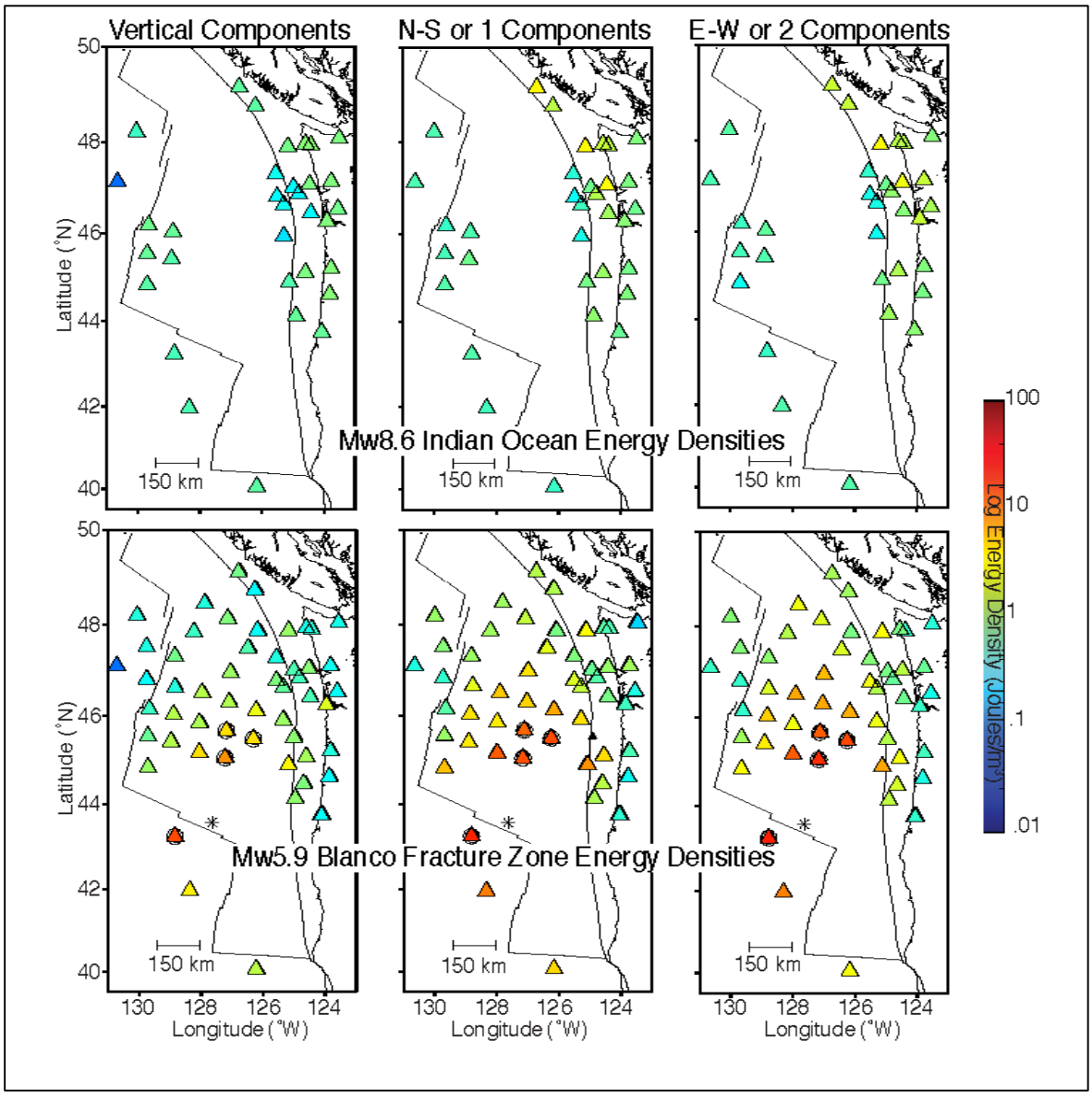

Figure S8. Energy densities for all 3 components of ground motion, for waves from the Mw8.6 Indian Ocean and Mw5.9 Blanco Fracture Zone. Figure format and processing steps are the same as for Figure S6. Note the increased densities at sites on the accretionary prism for both the horizontal components, particularly for the Indian Ocean waves. This increase also is apparent for the Blanco, comparing sites equidistant from the source but on and off the prism.

Figure S9

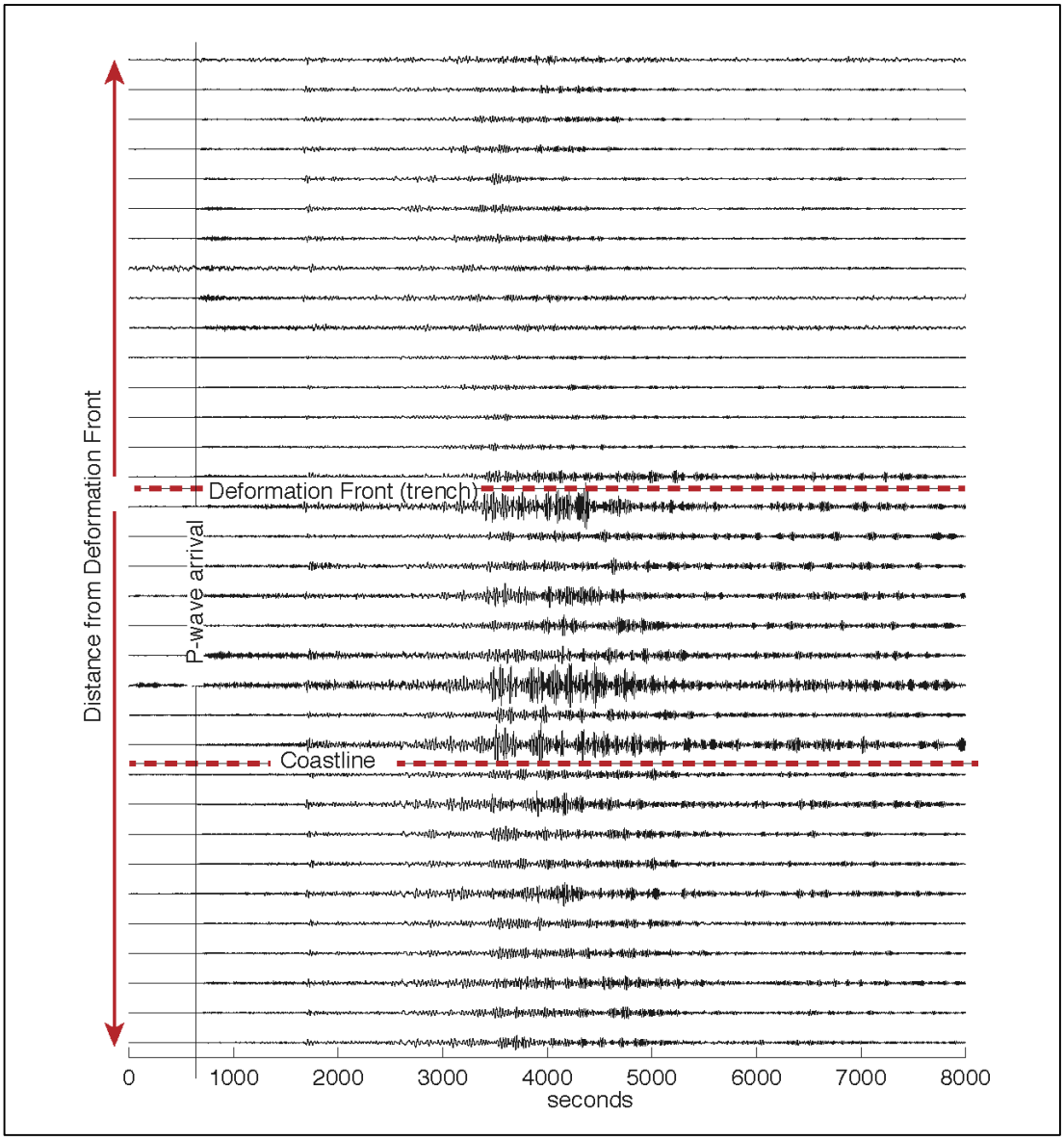

Figure S9. Ground velocities recorded as waves from the M_w8.6 Indian Ocean earthquake traversed the CI network. Either N-S or components identified as 1 are plotted, arranged in the order of increasing distance from the Cascadia deformation front (trench). Note the abrupt increase in amplitudes going from seaward of the front onto the accretionary prism, and the long duration of the waves. We terminated these signals at 7400 seconds from the P-wave arrival, because waves from the M_w8.2 Indian Ocean event began to arrive (although were significantly smaller, as Fig. S5 shows).